Optical spectroscopy and visible stimulated emission of Dy^{3+} ions in monoclinic α-$KY(WO_4)_2$ and α-$KGd(WO_4)_2$ crystals

Alexander A. Kaminskii*
Institute of Crystallography, Russian Academy of Sciences, 117333 Moscow, Russia

John B. Gruber†
Department of Physics, San Jose State University, San Jose, California 95192-0106

Sergei N. Bagaev
Institute of Laser Physics, Russian Academy of Sciences, 630090 Novosibirsk, Russia

Ken-ichi Ueda‡
Institute for Laser Science, University of Electro-Communications, Tokyo 182-8585, Japan

Uwe Hömmerich, Jae Tae Seo, and Doyle Temple
Research Center for Optical Physics, Department of Physics, Hampton University, Hampton, Virginia 23688

Bahram Zandi
ARL/Adelphi Laboratory Center, Adelphi, Maryland 20783-1197

Aleksei A. Kornienko and Elena B. Dunina
Department of Physics, Vitebsk Pedagogical Institute, Vitebsk 210036, Belarus

Aleksei A. Pavlyuk, Rima F. Klevtsova, and Fedor A. Kuznetsov
Institute of Inorganic Chemistry, Russian Academy of Sciences, 630090 Novosibirsk, Russia
(Received 30 July 2001; revised manuscript received 9 October 2001; published 13 March 2002)

The complex crystallographic, spectroscopic, and laser properties of Dy^{3+} ions in α-$KY(WO_4)_2$ and α-$KGd(WO_4)_2$ single crystals are investigated. Individual Stark levels for many of the $^{2S+1}L_J$ manifolds of Dy^{3+} ($4f^9$) ions in these monoclinic tungstates are obtained from luminescence and absorption spectra up to $\approx$28 000 cm^{-1} at $\approx$15 K. A crystal-field splitting analysis for the majority of these manifolds is performed. The rms deviation between 73 experimental and calculated Dy^{3+} Stark levels for both crystals was $\approx$10 cm^{-1}. Theoretical calculations of intermanifold intensity parameters are carried out by methods using the Judd-Ofelt approach with regard to interconfiguration interaction. All luminescence channels originating from levels of the metstable $^4F(3)_{9/2}$ state are compared with measured data. Pulsed stimulated emission in the visible range at the wavelengths of two lasing channels $^4F(3)_{9/2}\rightarrow{}^6H_{13/2}$ and $^4F(3)_{9/2}\rightarrow{}^6H_{11/2}$ of Dy^{3+} ions are excited and identified. On the basis of observed spectroscopic data we determine the peak cross section for all observed induced transitions as well. We conclude that Dy^{3+}-doped monoclinic tungstates α-$KGd(WO_4)_2$ and α-$KY(WO_4)_2$ are very attractive crystalline materials for generating visible laser light.

DOI: 10.1103/PhysRevB.65.125108 PACS number(s): 78.45.+h

I. INTRODUCTION

The laser properties of a family of monoclinic α-$KR(WO_4)_2$ tungstates doped with triply ionized lanthanides Ln^{3+} (where R=Y and Ln) were discovered at the Russian Academy of Sciences more then 30 years ago.[1] During these past decades, the generation of stimulated emission (SE) in these crystals was excited in different inter-Stark transitions for a great number of intermanifold $4f^N$-$4f^N$ channels (Fig. 1). At present the list of these crystals and their Ln^{3+}-ion activators is quite extensive (Table I). Rubidium neodymium tungstate $RbNd(WO_4)_2$ is also related to this family of lasing compounds.[17] Among all known Nd^{3+}-doped insulating lasing crystals,[18,19] α-$KGd(WO_4)_2$:Nd^{3+} demonstrates the highest SE generation performance ($^4F_{3/2}\rightarrow{}^4I_{11/2}$ channels) at low pumping energies with both lamp and laser-diode excitations (see, for example, Refs. 20–27, and references therein). Recently, the authors of Ref. 28 showed that mode-locked diode-pumped Yb^{3+}:$KGd(WO_4)_2$ crystals are very attractive for femtosecond lasers as well. Monoclinic α-$KR(WO_4)_2$ tungstates also have large nonlinear optical susceptibilities $\chi^{(3)}$, and therefore can be used in various laser experiments and applications that are based on the phenomena of stimulated Raman scattering (SRS).[29–36] For example, a highly efficient room-temperature practical eye-safe self-SRS Nd^{3+}:$KGd(WO_4)_2$ laser was designed,[37] where the first Stokes emission at $\approx$1.53-μm wavelength is the result of the intercavity interaction of the high-density fundamental SE field ($^4F_{3/2}\rightarrow{}^4I_{13/2}$ channel) associated with generating Nd^{3+} activators within this crystal-host, having a sufficient $\chi^{(3)}$ nonlinearity. In these $\chi^{(3)}$-active tungstates narrow absorption lines of

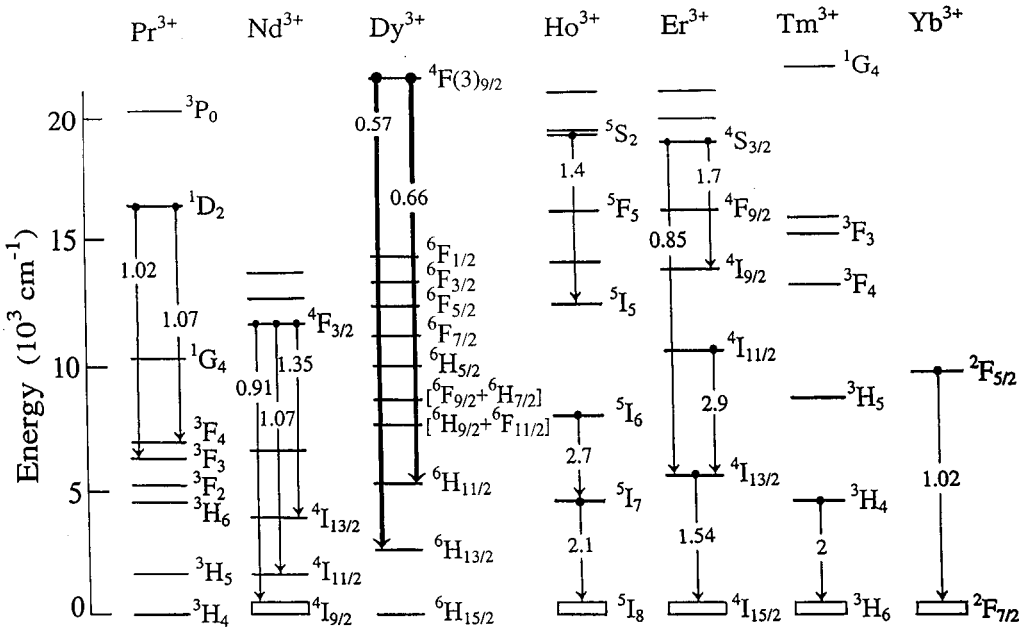

FIG. 1. Laser intermanifold $4f^N$-$4f^N$ transitions of lasing Ln^{3+}-activator ions in monoclinic α-$KLn(WO_4)_2$-type crystals. The ranges of SE channels are given in μm. SE transitions investigated in this paper are shown by thick arrows.

Ln^{3+} ions can also prevent undesirable cascade SRS processes.

α-$KR(WO_4)_2$:Ln^{3+} compounds have been the subject of comprehensive investigations of crystal-field splitting and intermanifold and inter-Stark transition intensities of Ln^{3+}-activator ions.[38–48] In the past, in these spectroscopic and laser investigations experts focused their attention mainly on the near and mid-IR SE channels of Ln^{3+} ions in these tungstates. At present, for example, due to actual applications for lidar systems for the remote sensing of ozone, there has arisen an interest in visible crystalline lasers which have directly excited SE wavelengths that can be doubled to yield UV wavelengths in the 0.27–0.32-μm region. Presently, it is known[19] that several various kinds of hosts with Ln^{3+} activators (Pr^{3+}, Tb^{3+}, Sm^{3+}, Ho^{3+}, Er^{3+}, and Tm^{3+}) can generate the required visible wavelengths. Unfortunately, compared to monoclinic α-$KR(WO_4)_2$ tungstates, which are already commercially available, most of these laser crystals are not easily accessible due to the difficulty in growing these materials with perfect optical quality. Recently, however, on the basis of our preliminary spectroscopic and SE experiments we concluded that, for the purposes indicated, some of the Dy^{3+}-doped crystals of the above-mentioned family of monoclinic tungstates, which are already commercially available, could be very attractive.

The electronic $4f^9$ configuration of Dy^{3+} ions gives rise to a large number of closely located $^{2S+1}L_J$ manifolds[49,50] resulting in a very tangled picture of their crystal-field splitting. Therefore, in understanding the different processes, including laser action in optically excited Dy^{3+}-doped crystals, it is particularly important to have a reliable determination of their Stark-level energies. Such detailed investigations were performed, to our knowledge, for only a very few crystals containing trivalent dysprosium.[51] Among these only one is known as a lasing compound: LaF_3:Dy^{3+}.[52,53] In the present work, we present results from precise spectroscopic measurements and crystal-field (CF) theoretical analyses of absorption and luminescence spectra of Dy^{3+}-doped laser α-$KY(WO_4)_2$ and α-$KGd(WO_4)_2$ monoclinic crystals. Our investigations provide us with the possibilities to make assignments to all registered visible SE wavelengths, and to determine the main intensity emission parameters as inter-

TABLE I. Known laser monoclinic double potassium rare-earth tungstates and their Ln^{3+} lasing ions.

Crystal	Ln^{3+} lasing ions						
	Pr^{3+}	Nd^{3+}	Dy^{3+}	Ho^{3+}	Er^{3+}	Tm^{3+}	Yb^{3+}
α-$KY(WO_4)_2$	Refs. 14 and 15	Refs. 1 and 2	Ref. 16	Refs. 3 and 9	Refs. 3 and 5	Ref. 15	Refs. 13
α-$KY_{0.5}Er_{0.5}(WO_4)_2$					Ref. 5		
α-$KGd(WO_4)_2$	Ref. 12	Ref. 3	Ref. 16	Refs. 4 and 5	Ref. 4	Ref. 15	Ref. 13
α-$KEr(WO_4)_2$					Refs. 7 and 11		
α-$KLu(WO_4)_2$		Ref. 8		Refs. 8 and 10	Ref. 6		
α-$KYb(WO_4)_2$						[a]	

[a]Unpublished data.

TABLE II. Some physical properties of the monoclinic α-$KY(WO_4)_2$ and α-$KGd(WO_4)_2$ single crystals.

Characteristic[a]	α-$KY(WO_4)_2$		α-$KGd(WO_4)_2$	
Space group	C_{2h}^6-C2/c or C_{2h}^6-$I2/c$ ($N15$)			
Unit-cell parameters (Å)	$C2/c$	$I2/c$	$C2/c$	$I2/c$
	$a=10.64$	$a=8.05$	$a=10.65$	$a=8.09$
	$b=10.35$	$b=10.35$	$b=10.37$	$b=10.37$
	$c=7.54$	$c=7.54$	$c=7.58$	$c=7.58$
	$\beta=130.5°$	$\beta=94°$	$\beta=130.75°$	$\beta=94.43°$
Cell volume ($Å^3$)	631.4		637.8	
Formula units per cell	$Z=4$			
Linear optical classification	biaxial			
Density (g/cm^3)	5.565		7.216	
Lasing Ln^{3+}-activator ions	Pr^{3+}, Nd^{3+}, Dy^{3+}, Ho^{3+}, Er^{3+}, Tm^{3+}, and Yb^{3+}			
Crystallographic positions of atoms and their oxygen coordination	C_2 for $K(12)$; Y, Gd and Ln(8); C_1 for W(4) and O			
Melting temperature (°C)	≈1080		≈1075	
Temperature of a polymorphic phase transition (°C)[b]	≈1015		≈1005	
Temperature of the crystallization (°C)	⩽1000			
Growth methods	Low-gradient Czochralski[c] Bridgman-Stockbarger[c] top-nucleated floating flax			
Specific heat (J/Kg grad)	≈500			
Thermal conductivity (W/cm grad)	≈0.03		$0.028_{[100]}$ $0.025_{[010]}$ $0.035_{[001]}$	
Thermal expansion (10^{-6}/grad)	≈4.6		$4_{[100]}$ $3.6_{[010]}$ $8.5_{[001]}$	
Hardness: Mhos scale	4.5–5			
Knoop scale (Kg/mm^2)	-		$\approx 370_{[100]}$ $\approx 390_{[010]}$ $\approx 460_{[001]}$	
Young's modules (GPa)	-		$\sim 115_{[100]}$ $\approx 150_{[010]}$ $\approx 90_{[001]}$	
Optical transparency (μm)[d]	≈0.34–≈5.5			
Energy gap (eV)	≈3.83			
Sellmeier equation for refractive indices	$n_i^2-1=K_i\lambda^2/(\lambda^2-\lambda_i^2)$[e]		$n_i=A_i+B_i/(C_i/\lambda)^2-D_i\lambda^{2}$[f]	
$dn/dT(10^{-6}$/grad)	≈0.4			
Phonon spectra extension (cm^{-1})[g]	≈905		≈901	
SRS-active vibration modes (cm^{-1})	$\omega_{R1}=905$		$\omega_{R1}=901$	
	$\omega_{R2}=765$		$\omega_{R2}=768$	
	$\omega_{R3}\approx 87$		$\omega_{R3}\approx 84$	
Steady-state Raman gain coefficient (cm/GW)[h]	≈3.6 for ω_{R1} and ω_{R2}		≈4.4[i] for ω_{R1} ≈3.3 for ω_{R2}	

manifold and inter-Stark luminescence branching ratios, as well as peak cross sections of the observed laser transitions. To assist the reader in understanding the many details that follow, we have organized the paper in the following manner: Section II describes some of the physical properties of α-$KY(WO_4)_2$ and α-$KGd(WO_4)_2$ single crystals, including their structure and conditions for growth. In Sec. III we give a brief description of the instrumentation and experimental analyses of the numerous absorption and luminescence spectra in the form of empirical crystal-field splitting schemes of the $^{2S+1}L_J$ multiplet manifolds of Dy^{3+} activators in these tungstates. The theoretical formalism and the calculation of

TABLE II. (*Continued.*)

n_i	K_i		λ_i (μm)	
n_p	2.813 49		0.152 906	
n_m	2.956 83		0.159 185	
n_g	3.127 83		0.161 512	
n^-	2.966 04		0.157 844	
n_i	A_i	B_i	C_i (nm)	D_i (nm^{-2})
n_p	1.5344	0.6573	186.18	2.0999×10^{-9}
n_m	1.5437	0.4541	188.91	2.1567×10^{-9}
n_g	1.3867	0.4360	170.02	0.2913×10^{-9}

[a]The majority of characteristics are given for the crystallographic $C2/c$ arrangement setting.
[b]Polymorphic transition to the β-orthorhombic phase with space group C_{2h}^{14}-$Pbna$.
[c]Flax adopted.
[d]For a 1-mm-thick sample.
[e]Room-temperature Sellmeier equation parameters for the principal refractive indices n_p, n_m, and n_g and for averaged refractive index n^- of α-KY$(WO_4)_2$. (Ref. 55).
[f]Room-temperature Sellmeier equation parameters for the principal refractive indices n_p, n_m, n_g of α-KGd$(WO_4)_2$ (Ref. 47). Here and as well as in the previous footnote (e), n_g is the tradition labeling of the highest refractive index of the optical indicatrix approximately along the crystallographic [001] direction (see Fig. 2), n_m is the intermediate refractive index along the $\approx$[100] direction, and n_p is the smallest refractive index exactly along the [100] direction of these monoclinic tangstates.
[g]From spontaneous Raman-scattering spectra.
[h]Due to the strong optical anisotropy of these crystals, only the highest values of g_{ssR} coefficients for the first Stokes generation under picosecond 1-μm Nd^{3+}:$Y_3Al_5O_{12}$ laser pumping are listed (Ref. 56).
[i]According to Ref. 57, $g_{ssR}\approx6$ cm/GW.

the crystal-field splitting, and comparisons with data, are given in Sec. IV. The measurement and calculation of intensity luminescence characteristics of Dy^{3+} ions in α-KY$(WO_4)_2$ and α-KGd$(WO_4)_2$ crystals in the approximation of weak and intermediate interconfiguration $4f$-$5d$ interactions are described in Sec. V. The laser experiments and the results of the identification of observed visible SE wavelengths are described in Sec. VI. We conclude the paper with a short summary.

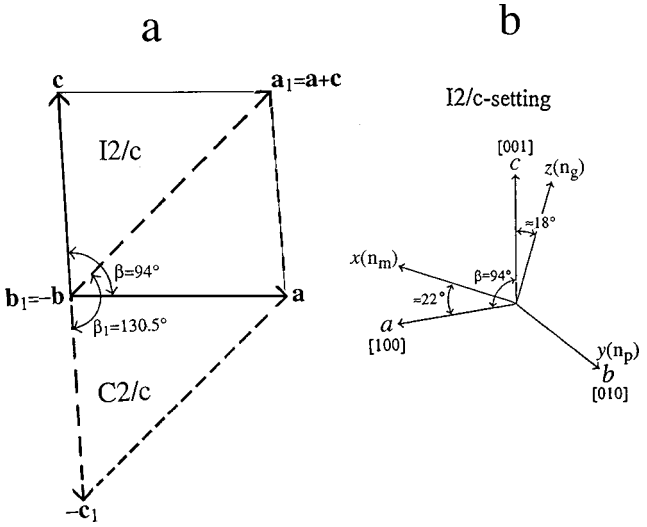

FIG. 2. (a) Connection of the basis vectors of the monoclinic α-KY$(WO_4)_2$ cell in crystallographic settings $I2/c$ (**a**,**b**,**c**) and $C2/c$ ($\mathbf{a}_1$,$\mathbf{b}_1$,$\mathbf{c}_1$). (b) The directions of the principal axes (x, y, z) of the optical indicatriz (the **b** vector is perpendicular to the plane of the drawing and points away from the observer, and $\mathbf{b}_1$ points toward the observer; also see the explanation in the text).

II. CRYSTALS FOR INVESTIGATIONS

Due to the occurrence of a polymorphic α-β transition near the melting point (see Table II), single crystals of the monoclinic compound α-K$R(WO_4)_2$ can be obtained only by a growth from the flux (see, for example, Refs. 1, 6–8, 14, 38, and 54) that is sufficiently large (several centimeters in size) for laser and SRS experiments; these include a number of other isostructural double alkali rare-earth tungstates. The marked solubility of α-K$R(WO_4)_2$, in particular α-KY$(WO_4)_2$ and α-KGd$(WO_4)_2$, in a melt of potassium di-tungstate $K_2W_2O_7$ makes it possible to crystallize them below the phase transition point by a low-gradient Czochralski technique (modified top-seeded solution method). The optimal conditions for the growth of Dy^{3+}-doped KY$(WO_4)_2$-KDy$(WO_4)_2$ and KGd$(WO_4)_2$-KDy$(WO_4)_2$ are obtained from phase diagrams. These tungstates were grown in Pt crucibles using oriented seeds along the crystallographic b axis. They were pulled at the rate of about 5 mm per day, and rotated at 50–90 rpm in an apparatus with a two-zone heater and a precise temperature control (±0.1 °C). The morphology habit of grown boules are formed mainly as faces of the {100}, {010}, and {001} pinacoids and the {110} and {011} prisms. For the series of single crystals

TABLE III. Coordinates of basic atoms in α-$KY(WO_4)_2$ and α-$KGd(WO_4)_2$ single crystals.

Atoms	Position	Coordinate					
		For $C2/c$			For $I2/c$		
		x_1/a	y_1/b	z_1/c	x/a	y/b	z/c
				α-$KY(WO_4)_2$			
W	$8f$	0.1962	0	0.2359	0.1962	0	0.4603
Y	$4e$	0	0.2725	0.75	0.50	0.2275	0.75
K	$4e$	0	0.692	0.75	0.50	0.808	0.75
O_1	$8f$	0.122	0.580	0.174	0.3727	0.080	0.552
O_2	$8f$	0.029	0.108	0.976	0.0242	−0.108	0.053
O_3	$8f$	0.222	0.342	0.120	0.2740	−0.158	0.398
O_4	$8f$	0.185	0.927	0.930	0.1882	0.073	0.255
				α-$KGdY(WO_4)_2$[a]			
W	$8f$	0.1948	0.0001	0.2359	0.1948	0.0001	0.4589
Gd	$4e$	0	0.2716	0.75	0.50	0.2284	0.75
K	$4e$	0	0.6921	0.75	0.50	0.8079	0.75
O_1	$8f$	0.1273	0.5764	0.1861	0.3727	0.0764	0.5588
O_2	$8f$	0.0242	0.1074	0.9727	0.0242	−0.1074	0.0515
O_3	$8f$	0.2260	0.3407	0.1284	0.2740	−0.1593	0.4024
O_4	$8f$	0.1882	0.9242	0.9390	0.1882	0.0758	0.2492

[a]For the $C2/c$ setting of the α-$KGd(WO_4)_2$, also see Ref. 47. Very useful data for the α-$KDy(WO_4)_2$ crystal are also given in Ref. 44.

obtained by this means, α-$KY_{1-x}Dy_x(WO_4)_2$ and α-$KGd_{1-x}Dy_x(WO_4)_2$ ($x=0.001-0.03$) of satisfactory optical quality are obtained. For SE measurements experimental samples are fabricated as plates having different thicknesses and rods of up to 45 mm in length and ≈5.5 mm in diameter. The plane-parallel (≈10 arc secs) end faces of these plates have no antireflection coatings.

The low-temperature tungstates α-$KY(WO_4)_2$ and α-$KGd(WO_4)_2$ crystallize in the monoclinic centrosymmetric space group C_{2h}^6-$C2/c$ or C_{2h}^6-$I2/c$, with cell parameters which are shown in Table II. The second $I2/c$-arrangement setting is more attractive because its parameters, including the monoclinic angles $\beta \approx 94°$, are incomparably better to correlate with the morphology gabit of flux used to grow these crystals. This significantly simplifies our efforts to cut them out as oriented samples. That is why, for the fabrication of our oriented samples, we used the $I2/c$ setting. However, the $C2/c$ space group is recommended by the International Crystallographic Union as the standard setting.[58] Unfortunately, different authors used both these settings. This causes some problems for readers. Therefore, we considered it essential to give the crystallographic axis transformation in these two settings. The basis vectors $(\mathbf{a}_1, \mathbf{b}_1, \mathbf{c}_1)$ and $(\mathbf{a}, \mathbf{b}, \mathbf{c})$ of the monoclinic unit cell in the $C2/c$ and $I2/c$ arrangement settings [correspondingly, of the α-$KY(WO_4)_2$ and α-$KGd(WO_4)_2$ structures] are shown in Fig. 2, with corresponding atom coordinates related to each other, as

$$\mathbf{a}_1 = \mathbf{a} + \mathbf{c}, \qquad \mathbf{b}_1 = -\mathbf{b}, \qquad \mathbf{c}_1 = -\mathbf{c} \tag{1}$$

and

$$\begin{bmatrix} x \\ y \\ z \end{bmatrix} = \begin{bmatrix} 1 & 0 & 0 \\ 0 & -1 & 0 \\ 1 & 0 & -1 \end{bmatrix} \begin{bmatrix} x \\ y_1 \\ z_1 \end{bmatrix}. \tag{2}$$

In addition, the coordinates of the basic atoms and corresponding principal inter-atomic distances in α-$KY(WO_4)_2$ and α-$KGd(WO_4)_2$ structures for both crystallographic settings are summarized in Tables III and IV. In addition to these data, Fig. 3 shows some crystal structure fragments which are illustrative of the atomic constitution of these monoclinic tungstates in the form of polyhedrons. As may be inferred from Tables III and IV, as well as from Fig. 3, the crystal structure of the monoclinic α-$KR(WO_4)_2$ tungstates contains three different type of polyhedrons. The tungsten and oxygen atoms occupy $8f$ positions, forming six coordinated polyhedrons of C_1 symmetry which can be presented as highly distorted octahedrons. The K and R atoms (in our case $R=$ Y and Gd) are placed at $4e$ positions, with the C_2 local symmetries being eight and 12, coordinated by the oxy-

TABLE IV. Principal interatomic distances in α-$KY(WO_4)_2$ and α-$KGd(WO_4)_2$ single crystals (in Å).

Octahedron WO_6		Polyhedron YO_8		Polyhedron KO_{12}	
		α-$KY(WO_4)_2$			
W-O_1	1.78	Y-O_1 (×2)	2.31	K-O_4 (×2)	2.84
W-O_4	1.72	Y-O_2 (×2)	2.28	K-O_4′ (×2)	2.86
W-O_3	1.84	Y-O_3 (×2)	2.31	K-O_1 (×2)	2.80
W-O_2	1.93	Y-O_3′ (×2)	2.71	K-O_2 (×2)	3.07
W-O_2′	2.14	⟨Y-O⟩	2.40	K-O_3 (×2)	3.12
W-O_4′	2.36			K-O_1′ (×2)	3.31
⟨W-O⟩	1.96			⟨K-O⟩	3.00
		α-$KGd(WO_4)_2$[a]			
W-O_1	1.765	Gd-O_1 (×2)	2.332	K-O_4 (×2)	2.800
W-O_4	1.772	Gd-O_2 (×2)	2.297	K-O_4′ (×2)	2.858
W-O_3	1.843	Gd-O_3 (×2)	2.352	K-O_1 (×2)	2.893
W-O_2	1.950	Gd-O_3′ (×2)	2.690	K-O_2 (×2)	3.091
W-O_2′	2.094	⟨Gd-O⟩	2.418	K-O_3 (×2)	3.109
W-O_4′	2.344			K-O_1′ (×2)	3.280
⟨W-O⟩	1.961			⟨K-O⟩	3.005

[a]For the $C2/c$ setting of the α-$KGd(WO_4)_2$, also see Ref. 47. Very useful data for the α-$KDy(WO_4)_2$ crystal are also given in Ref. 44.

gen atoms. The *R* and K polyhedrons are depicted as distorted square antiprisms and distorted icosahedrons, respectively. The Dy^{3+} ions substituting for Y^{3+} or Gd^{3+} in the lattice of these tungstates form one type of activator centers.

III. INSTRUMENTATION AND SPECTROSCOPIC MEASUREMENTS

A precise determination of Stark-level energies, and a measurement of intensity characteristics as well as kinetic parameters of emitting intermanifold channels of Dy^{3+} ions in α-$KY(WO_4)_2$ and α-$KGd(WO_4)_2$ crystals, were carried out by the conventional methods of absorption and luminescence analysis. For spectroscopic measurements, at temperatures from ≈15 K to room temperature the oriented samples of these tungstates were mounted with plane-parallel sides perpendicular within 2° to their crystallographic axes *a*, *b*, and *c* (in the $I2/c$ setting) on a Cu cold-finger of a two-stage closed-cycle helium refrigerator (Advanced Research Systems, Model CSW-202). A standard for spectral irradiance tungsten incandescent lamp (Optronic Laboratories Inc., Model 220C) was employed as a broadband light source for absorption measurements. In a like manner the luminescence was dispersed by using a carefully calibrated 1-m grating monochromator (Acton Research Corp., Model AM510-Ml) and was detected with a cooling photomultiplier tube (Hamamatsu R928) for studies in the visible spectral region and with an $In_xGa_{1-x}As$ detector for IR measurements. For luminescence excitation we used the multiline UV output (0.334–0.364 μm) of an Ar-ion laser (Coherent, Model Sabre). Its emission was chopped at 17 Hz, and a lock-in (Stanford Research Systems, Model SR-510) technique was used for data acquisition. Temperature-dependent luminescence lifetime studies were performed with third-harmonic generation at a 0.355-μm wavelength of a nanosecond $Nd^{3+}:Y_3Al_5O_{12}$ laser (Continuum, Model SLII-10) using the same spectroscopic setup. The decay signal in the visible was detected and averaged using a digitized oscilloscope (Tektronix, Model TDS-420A). Room-temperature absorption spectra were taken with a UV-VIS-NIR spectrophotometer (Varian, Model Cary-5E).

A detailed analysis of the structure of the absorption and luminescence spectra, recorded at different temperatures, confirmed that Dy^{3+} ions can enter into monoclinic α-$KY(WO_4)_2$ and α-$KGd(WO_4)_2$ crystals in $4e$ eight-coordinated C_2 (see Tables II and III) sites and form one type of activator center. For the $4f^9$ electronic configuration the number of multiplet manifoilds $^{2S+1}L_J$ is 198 with a ground state $^6H_{15/2}$. Because the Dy^{3+} ion is a Kramers ion, each observed Stark level is twofold degenerate in a crystallographic position of C_2 symmetry. Due to the limited optical transparency of our tungstates (see Table II), we were able to investigate the Stark levels. For only a small part of these $^{2S+1}L_J$ manifolds. To demonstrate this important property of these crystals under study, below we present only part of the results obtained that are accompanied by a guiding diagram in Fig. 4. The diagram shows, in particular, that the Stark structure of many of the $^{2S+1}L_J$ states of Dy^{3+} ions in α-$KY(WO_4)_2$ and α-$KGd(WO_4)_2$ are derived from the separate analysis of each of the different $4f^9$-$4f^9$ intermanifold transitions. We thus obtain better accuracy and reliability of the results. That is of prime importance for both subsequent CF calculations and SE emission identification.

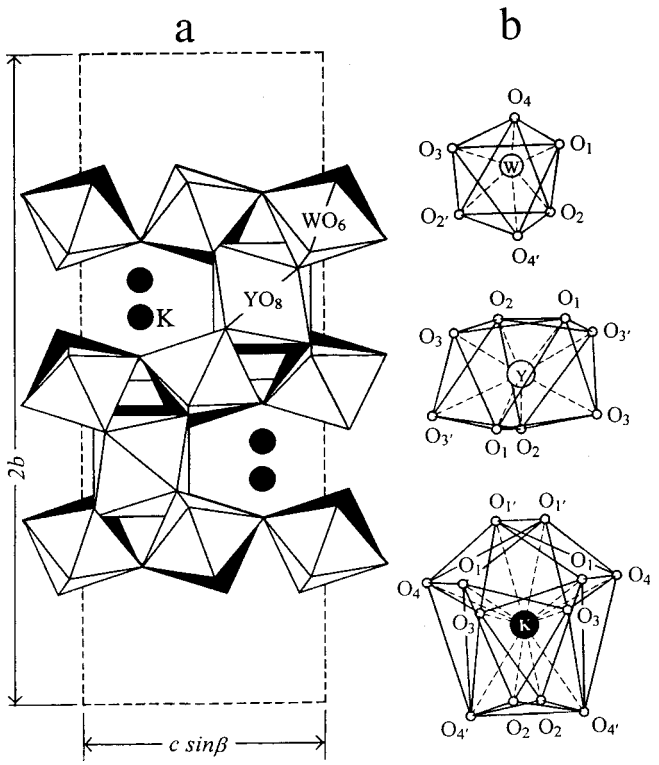

FIG. 3. Crystal structure of the monoclinic α-$KY(WO_4)_2$ tungstate: (a) Projection along *a* axis; the polyhedra of next level are shown by blacking. (b) Structure of WO_6, YO_8, and KO_{12} polyhedra; the distances of metal-oxygen are shown by dashed lines (see Table IV).

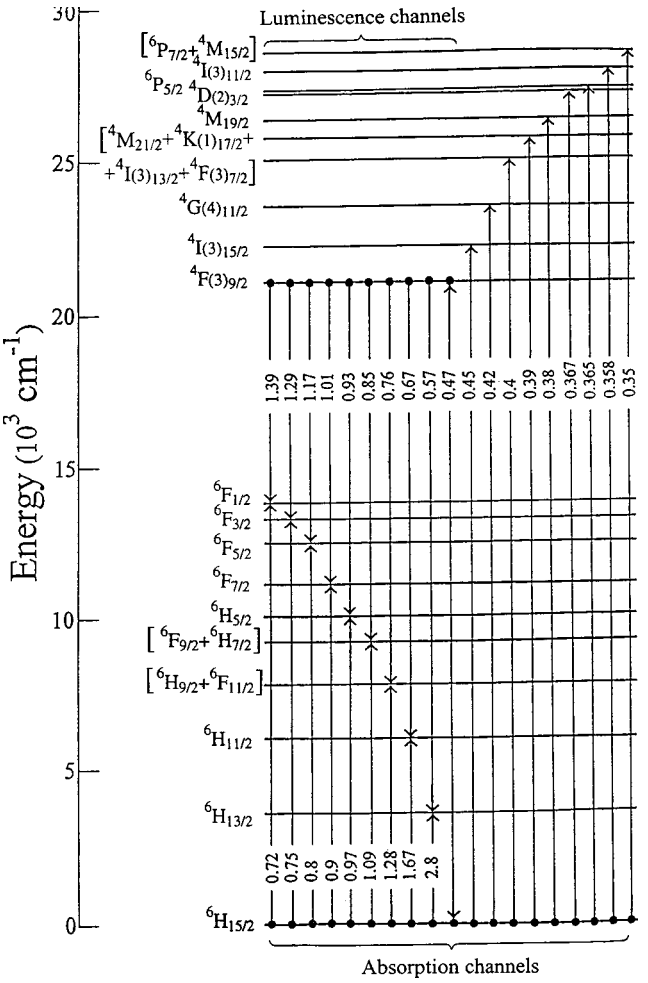

FIG. 4. Diagram of $^{2S+1}L_J$ states that guide the spectroscopic studies given below for Dy^{3+} ions in monoclinic α-$KY(WO_4)_2$ and α-$KGd(WO_4)_2$ crystals. The spectral ranges of intermanifold $4f^9$-$4f^9$ transitions are given in μm.

As expected, the Dy^{3+} ions in α-$KY(WO_4)_2$ and α-$KGd(WO_4)_2$ crystals offer one emitting $^4F(3)_{9/2}$ manifold with strong visible luminescence inter-Stark transitions. In this connection, we take particular care to conduct an analysis of its Stark levels, as well as of the Stark levels of the ground state $^6H_{15/2}$. The determination of the energies of these levels to a high accuracy helped us to carry out a reliable analysis of the Stark structure of other $^{2S+1}L_J$ manifolds of the activator ions in these laser tungstates. Figure 5 shows low-temperature resonant absorption $^6H_{15/2} \rightarrow {}^4F(3)_{9/2}$ and luminescence $^4F(3)_{9/2} \rightarrow {}^6H_{15/2}$ spectra together with a corresponding CF splitting scheme of the $^6H_{15/2}$ and $^4F(3)_{9/2}$ states in the case of α-$KY(WO_4)_2$ crystal. For the sake of clarity, all the lines in the spectra and inter-Stark transitions in the scheme have a corresponding connected numeration. We carried out an analysis of the temperature evolution of the visible luminescence which connects the Stark levels of the metastable $^4F(3)_{9/2}$ state and levels of the $^6H_{13/2}$ and $^6H_{11/2}$ manifolds, and found consistent support for the foregoing results. The temperature spectra together with the corresponding CF splitting schemes are given in Figs. 6 and 7. The selected luminescence spectra shown are obtained for a specific measurement geometry. This display is more informative as an explanation of the inter-Stark transitions in the corresponding CF splitting schemes. Despite the fact that the temperature broadening of the transitions due to strong electron-phonon interaction in our monoclinic tungstates, all observed luminescence peaks in these spectra are easily analyzed. We take note of the visible SE in α-$KY(WO_4)_2$ and α-$KGd(WO_4)_2$ crystals, and connect these luminescence channels to these spectra below, in Sec. V.

It is very important to have a detailed knowledge of the Stark-level energies of nonoverlapping $^6F_{1/2-7/2}$ states, so that a reliable fitting procedure can be established for CF calculations of Dy^{3+} ions in the crystals, since the manifold $^6F_{9/2\text{-}11/2}$ and the $^6F_{1/2}$ states are mixed with the levels of $^6H_{7/2,9/2}$ manifolds. Spectroscopic investigations of Dy^{3+}-doped crystals provided little information about the position of the Stark level of the $^6F_{1/2}$ state (see Ref. 51). Therefore, in our measurements we paid much attention to all levels of the $^6F_{1/2-7/2}$ manifolds of Dy^{3+} ions in α-$KY(WO_4)_2$ and α-$KGd(WO_4)_2$ tungstates. The data obtained are presented in Figs. 8–10, as illustrations of some of the absorption and luminescence spectra that we studied. All Stark levels of the $^6F_{1/2-7/2}$ multiplet manifolds for both crystals were observed and analyzed. In Figs. 11 and 12 we give the results of energy-level measurements for two groups of overlapping manifolds $[^6H_{9/2}+{}^6F_{11/2}]$ and $[^6H_{9/2}+{}^6F_{7/2}]$. These data are shown only for α-$KY(WO_4)_2$,

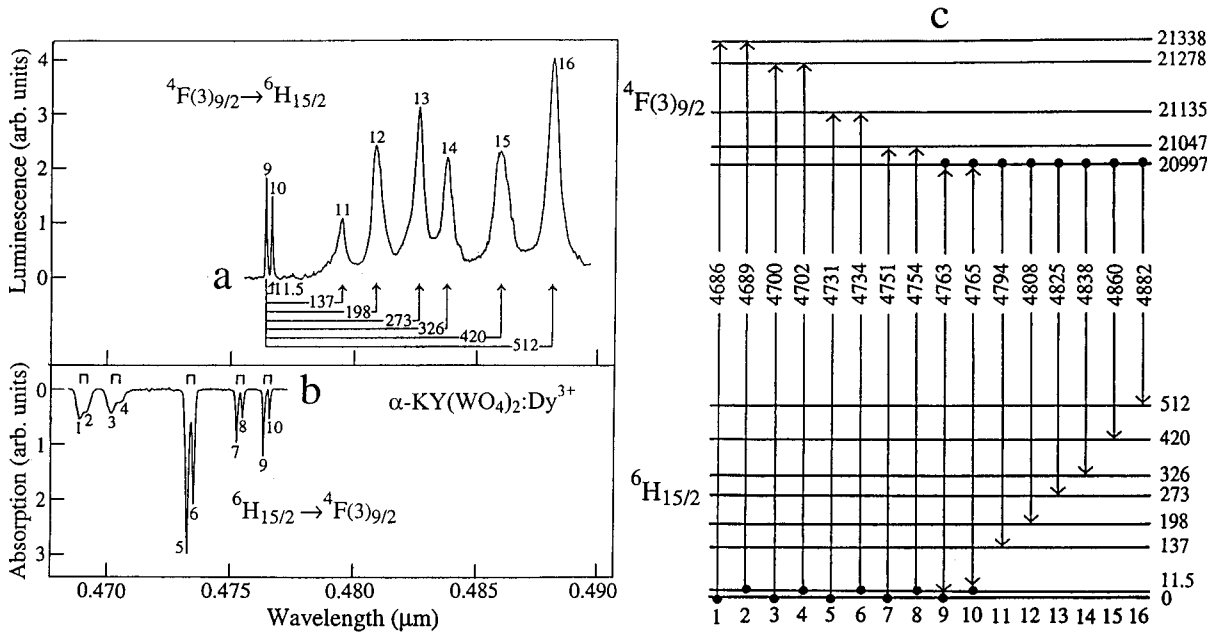

FIG. 5. (a) Unpolarized luminescence and (b) absorption spectra for the resonance intermanifold transition $^4F(3)_{9/2}\leftrightarrow{}^6H_{15/2}$, and (c) CF splitting scheme of the $^4F(3)_{9/2}$ and $^6H_{15/2}$ manifolds of Dy^{3+} ions in α-$KY(WO_4)_2$ crystal at ≈15 K. The arrows in the luminescence spectrum give (in cm^{-1}) the splitting of the ground state $^6H_{15/2}$, and the square brackets in the absorption spectrum indicate the energy gap (11.5 cm^{-1}) between two lowest Stark levels of the ground state $^6H_{15/2}$. Lines in the spectra and corresponding inter-Stark transitions in the scheme are denoted by the same numeration. The energy of each Stark level is given in cm^{-1}, and transitions between them are in Å.

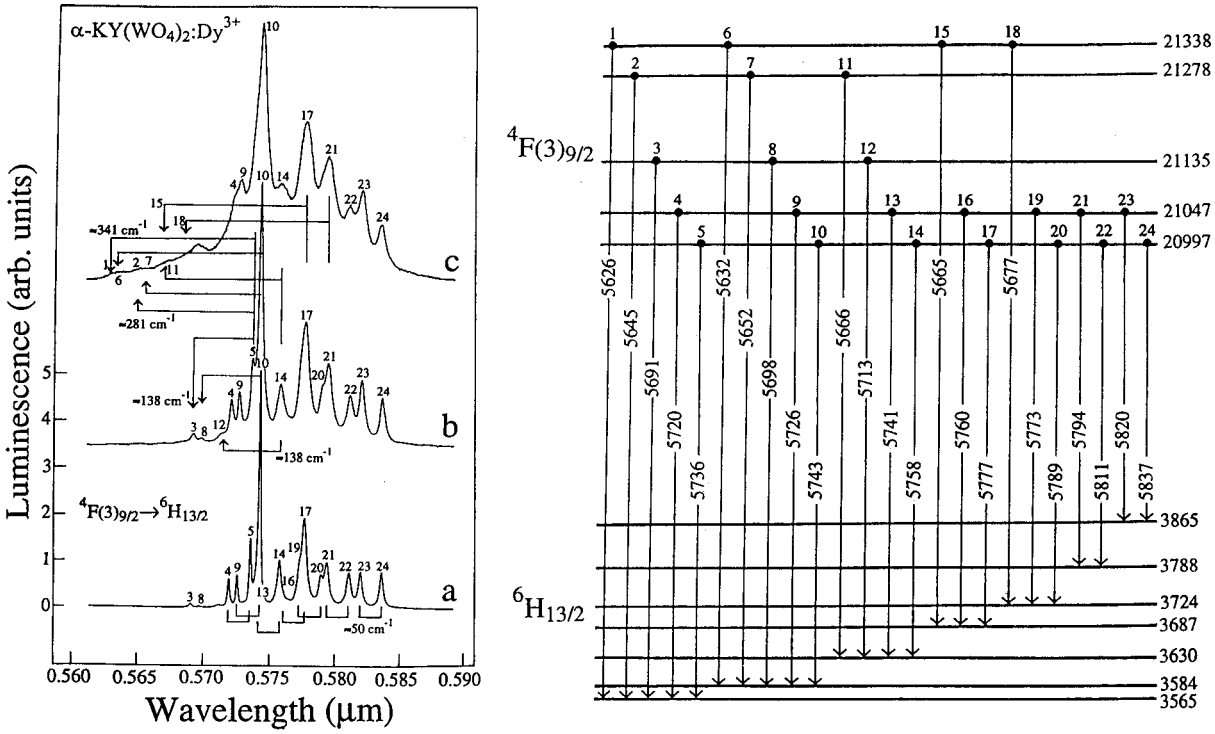

FIG. 6. Orientational luminescence spectra ($^4F(3)_{9/2}\rightarrow{}^6H_{13/2}$ channel, along the *a* axis) at (a) ≈15 K, (b) ≈80 K, and (c) ≈220 K, and the CF splitting scheme at ≈15 K of the $^4F(3)_{9/2}$ and $^6H_{13/2}$ manifolds of Dy^{3+} ions in an α-$KY(WO_4)_2$ crystal. The arrows in spectra (b) and (c) indicate lines connected with the inter-Stark transitions that originate from the third, fourth and fifth levels of the metastable $^4F(3)_{9/2}$ state, as well as the corresponding energy gaps between its first level and higher-lying levels. Square brackets in the (a) spectrum indicate the gap (50 cm^{-1}) between the two lowest Stark levels of the $^4F(3)_{9/2}$ manifold. Other notations are the same as in Fig. 5.

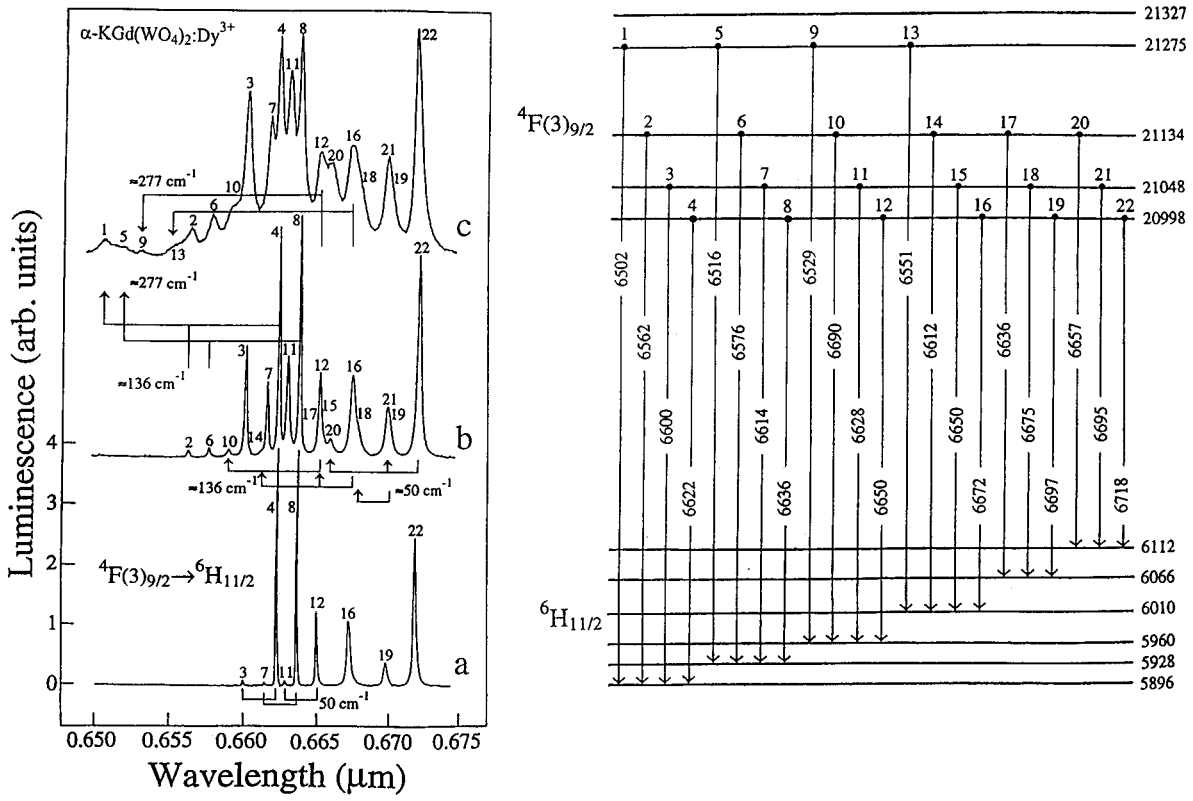

FIG. 7. Orientational luminescence spectra ($^4F(3)_{9/2} \rightarrow {}^6H_{11/2}$ channel, along the *c* axis) at (a) ≈15 K, (b) ≈80 K, and (c) ≈220 K, and the CF splitting scheme at ≈15 K of the $^4F(3)_{9/2}$ and $^4F(3)_{9/2}$ and $^6H_{11/2}$ manifolds of Dy^{3+} ions in an α-$KGd(WO_4)_2$ crystal. The arrows in spectra (b) and (c) indicate the lines are connected with inter-Stark transitions that originate from the second, third, and fourth levels of the metastable $^4F(3)_{9/2}$ state, as well as corresponding energy gaps between the first level and other higher-lying energy levels. Other notations are the same as in Figs. 5 and 6.

since absorption and luminescence properties in these spectral regions for Dy^{3+} ions in the α-$KGd(WO_4)_2$ crystal are very similar. We used only the absorption spectra for a determination of the energy levels of the quartet and sextet states $^{2S+1}L_J$, which have higher energies than the metastable $^4F(3)_{9/2}$ state. Figures 13 and 14 show results obtained from an analysis for two quartet states $^4I(3)_{15/2}$ and $^4G(4)_{11/2}$. Transitions to these states are expected during absorption in the blue spectral region for both monoclinic tungstates. It is important to give some data for several UV absorption transitions that were also investigated. Such results are presented in Figs. 15 and 16. The energies of all determined Dy^{3+}-ion Stark levels for α-$KY(WO_4)_2$ and α-$KGd(WO_4)_2$ crystals are listed in Table V.

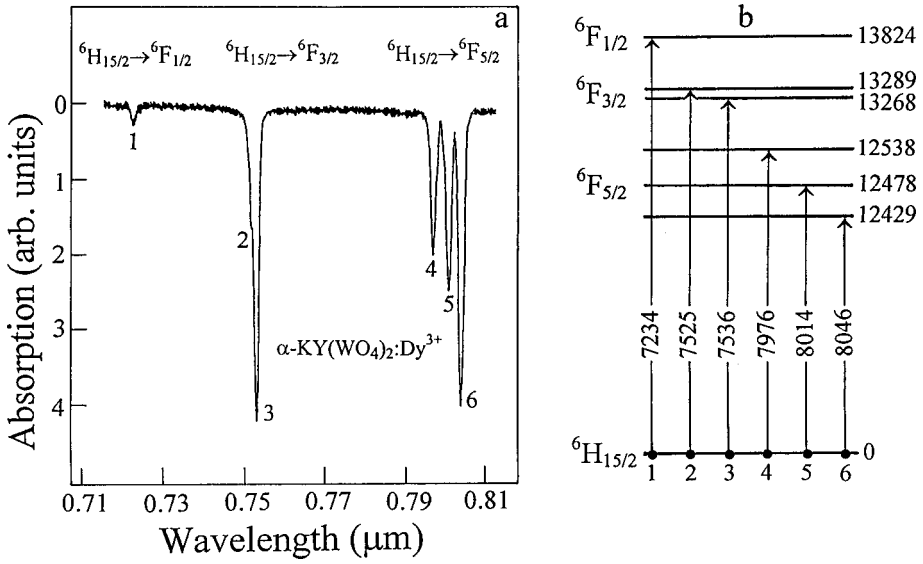

FIG. 8. (a) Unpolarized absorption spectra ($^6H_{15/2} \rightarrow {}^6F_{1/2\text{-}5/2}$ channels) and (b) CF splitting scheme of $^6F_{1/2}$, $^6F_{3/2}$, and $^6F_{5/2}$ manifolds of Dy^{3+} ions in an α-$KY(WO_4)_2$ crystal at ≈15 K. The notations are the same as in Fig. 5.

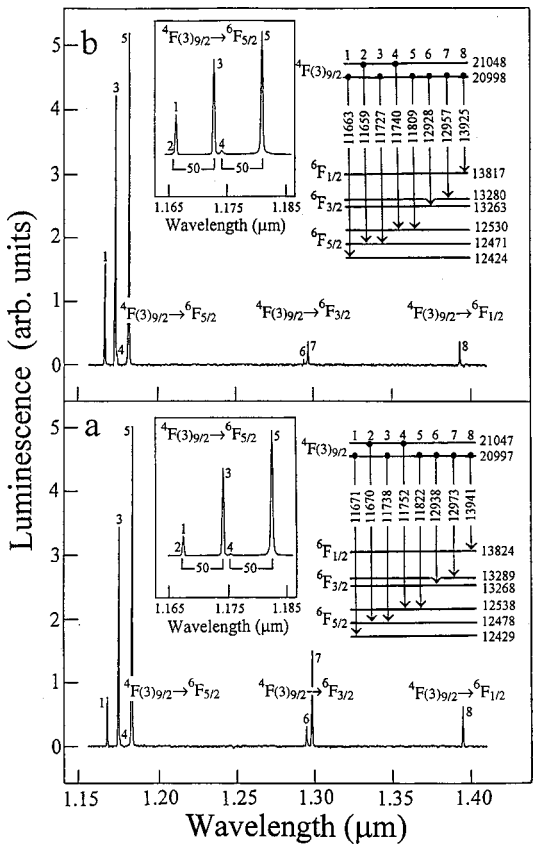

FIG. 9. Orientational luminescence spectra ($^4F(3)_{9/2}\rightarrow{}^6F_{1/2\text{-}5/2}$ channels, along the *c* axis) and CF splitting schemes of Dy^{3+} ions in (a) α-$KY(WO_4)_2$ and (b) α-$KGd(WO_4)_2$ crystals at ≈15 K. In the frames the details of these spectra are shown for the $^4F(3)_{9/2}\rightarrow{}^6F_{5/2}$ intermanifold transition, where the square brackets indicate the energy gap (50 cm^{-1}) between two lowest Stark levels of the metastable $^4F(3)_{9/2}$ state. Other notations are the same as in Figs. 5 and 6.

We observe $(J+1/2)$ Stark components for each of the expected $^{2S+1}L_J$ multiplet manifolds between 0 and ≈28 800 cm^{-1} with high accuracy for both monoclinic tungstates. Of these multiplets we chose the 15 lowest in energy for a detailed crystal-field splitting analysis involving the calculations given in Sec. IV.

IV. CRYSTAL-FIELD SPLITTING CALCULATIONS FOR Dy^{3+} ENERGY LEVELS

The initial CF splitting parameters were obtained from a point-charge lattice-sum model adapted to include effective ionic charges and dipole and quadrupole polarizabilities in parametrized form.[51,59] The details concerning the coordinate structures of the monoclinic α-$KY(WO_4)_2$ and α-$KGd(WO_4)_2$ tungstates are taken from Tables III and IV and Refs. 54 and 60. Dipole ionic polarizabilities and quadrupole polarizabilities were reported in several references.[61,62] The ionic charges can be parametrized and varied in order to obtain the best overall agreement between calculated and observed Stark levels. We found that using a formal charge on each ion in the lattice calculation led to the best agreement. Results of the CF splitting are given in Tables VI and VII.

The calculated CF components A_{nm}, given in Table VIII, are of the form

$$A_{nm}=-e^2\Sigma_j q_j[C_{nm}\langle \mathbf{r}_j\rangle/r_j^{n+1}], \tag{3}$$

where the sum is taken over all ions in the lattice. The B_{nm} parameters used to establish the splitting of the multiplet manifolds of Dy^{3+} activators $(4f^9)$, $^{2S+1}L_J$, in sites of C_2 symmetry, are determined using the three-parameter theory,[63]

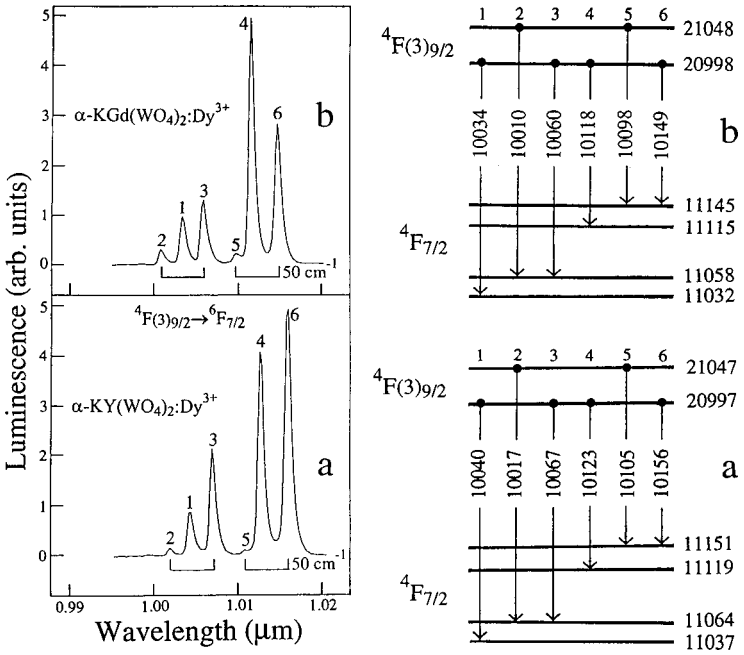

FIG. 10. Orientational luminescence spectra ($^4F(3)_{9/2}\rightarrow{}^6F_{7/2}$ channel, along the *c* axis) and CF splitting scheme of Dy^{3+} ions in (a) α-$KY(WO_4)_2$ and (b) α-$KGd(WO_4)_2$ crystals at ≈15 K. Square brackets in the spectra indicate the energy gap (50 cm^{-1}) between the two lowest Stark levels of the metastable $^4F(3)_{9/2}$ state. Other notations are the same as in Fig. 5.

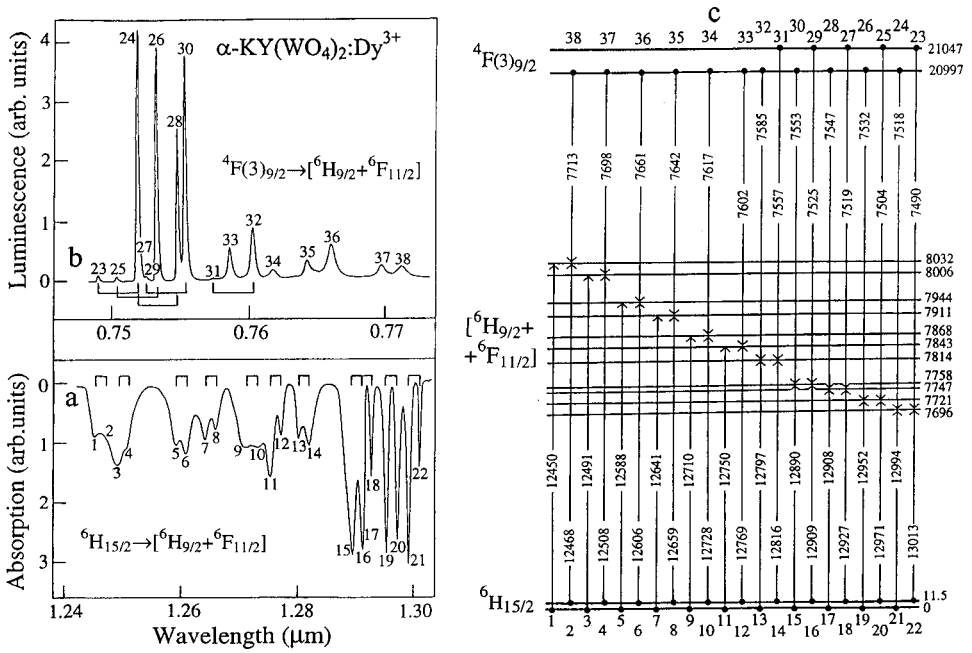

FIG. 11. (a) Unpolarized absorption ($^6H_{15/2}\rightarrow[^6H_{9/2}+{}^6F_{11/2}]$ channels) and (b) luminescence ($^4F(3)_{9/2}\rightarrow[^6H_{9/2}+{}^6F_{11/2}]$ spectra, as well as (c) the CF splitting scheme of the $^6H_{15/2}$, $[^6H_{9/2}+{}^6F_{11/2}]$, and $^4F(3)_{9/2}$ manifolds of Dy^{3+} ions in an α-$KY(WO_4)_2$ crystal at ≈15 K. Square brackets in the spectra indicate the energy-gap splitting between the two lowest Stark levels of the ground state $^6H_{15/2}$ (11.5 cm^{-1}) in the (a) spectrum and the metastable state $^4F(3)_{9/2}$ (50 cm^{-1}) in the (b) spectrum. Other notations are the same as in Fig. 5.

where

$$B_{nm}=\rho_n A_{nm}. \tag{4}$$

Values of ρ_2, ρ_4, and ρ_6 were given in Ref. 53 for all tripositive rare-earth ions. ρ_n include corrections to the $\langle r^n\rangle$ values when the ions are incorporated into solids, as well as shielding factors due to the localized nature of the $4f^N$ orbitals. For Dy^{3+} ions ($4f^9$) $\rho_2=0.1681$, $\rho_4=0.4341$, and $\rho_6=1.0614$. The units for all parameter values are given in Table VIII.

The Hamiltonian for the CF splitting is given as

$$\hat{H}_{\rm CF}=\Sigma_{n\ \rm even}\Sigma_{m=-n}^{n}B_{nm}^{*}\Sigma_{i=1}^{N}C_{nm}(\hat{\mathbf{r}}_i), \tag{5}$$

where B_{nm} are the CF parameters and

$$B_{nm}^{*}=(-1)^m B_{n,-m}. \tag{6}$$

$C_{nm}(\hat{r}_i)$ are one-electron spherical tensors, related to ordinary spherical harmonics $Y_{nm}(\Theta_i\phi_i)$ by

$$C_{nm}(\hat{\mathbf{r}}_i)=[4\pi/(2n+1)]^{1/2}Y_{nm}(\Theta_i\phi_i), \tag{7}$$

where Θ_i and ϕ_i are polar coordinates of the ith $4f^N$ electrons. In Eq. (5), the sums on n and m run over 2, 4, and 6, with $m=0,\pm2,\pm....$, as is appropriate for C_2 symmetry with the C_2 axis chosen as the quantization axis. B_{nm} are, in general, complex except for the B_{n0}, which are real. In addition, we assume that the coordinate system has been rotated about the C_2 axis, so that B_{22} is real.

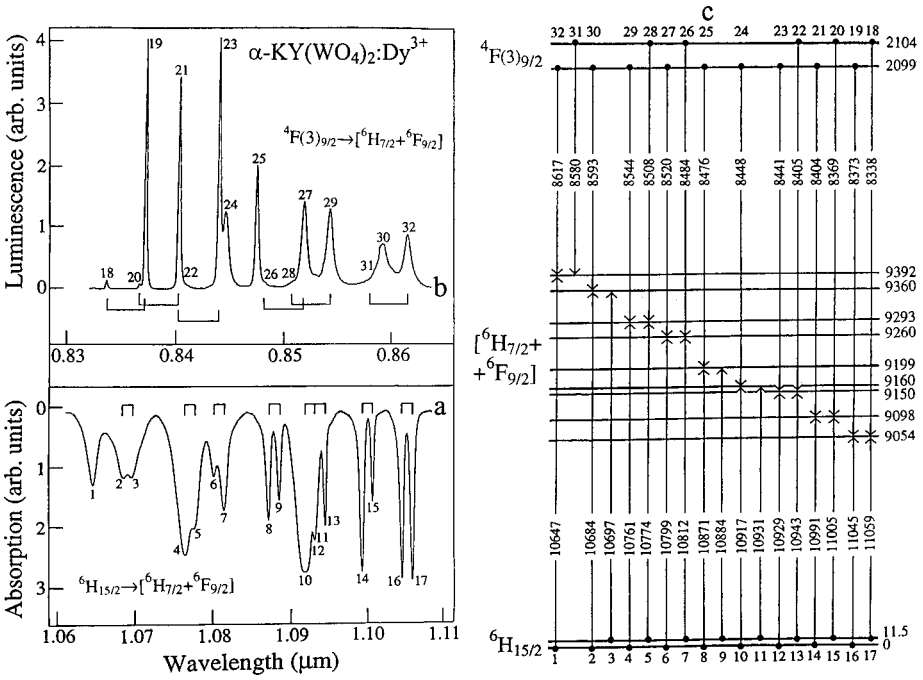

FIG. 12. (a) Unpolarized absorption ($^6H_{15/2}\rightarrow[^6H_{7/2}+{}^6F_{9/2}]$ channels) and (b) luminescence ($^4F(3)_{9/2}\rightarrow[^6H_{9/2}+{}^6F_{7/2}]$) spectra, as well as (c) the CF splitting scheme of the $^6H_{15/2}$, $[^6H_{9/2}+{}^6F_{7/2}]$, and $^4F(3)_{9/2}$ manifolds of Dy^{3+} ions in an α-$KY(WO_4)_2$ crystal at ≈15 K. Square brackets in the spectra indicate the energy-gap splitting between the two lowest Stark levels of the ground state $^6H_{15/2}$ (11.5 cm^{-1}) in the (a) spectrum and the metastable state $^4F(3)_{9/2}$ (50 cm^{-1}) in the (b) spectrum. Other notations are the same as in Fig. 5.

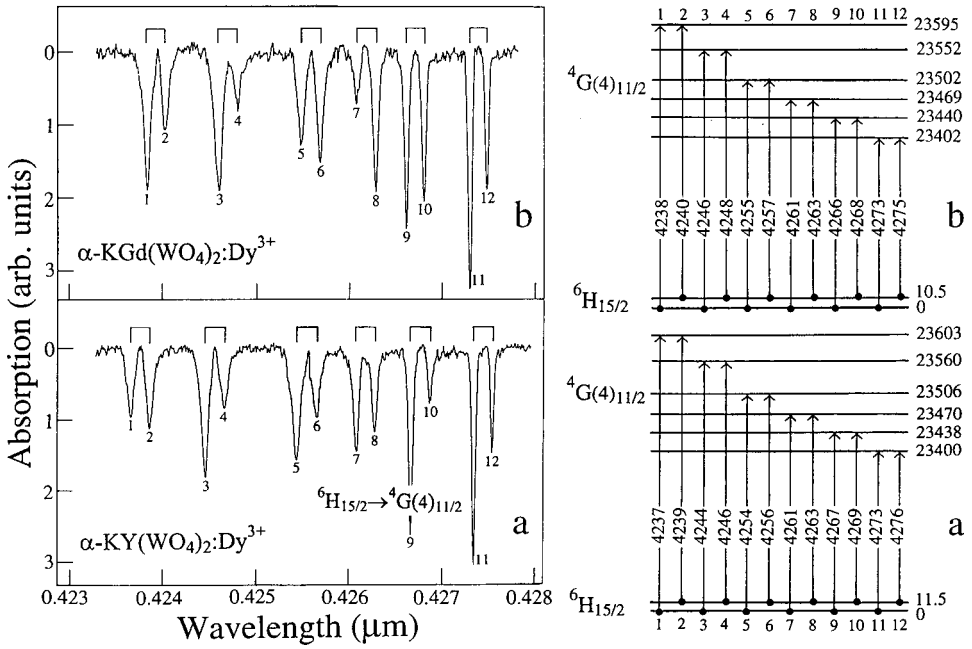

FIG. 13. Unpolarized absorption spectra ($^6H_{15/2}\rightarrow{}^4G(4)_{11/2}$ channel) and CF splitting schemes of the $^6H_{15/2}$ and $^4G(4)_{11/2}$ manifolds of Dy^{3+} ions in (a) α-$KY(WO_4)_2$ and (b) α-$KGd(WO_4)_2$ crystals at $\approx$15 K. Square brackets in the spectra indicate the energy gap splitting between the two lowest Stark levels of the ground state $^6H_{15/2}$. Other notations are the same as in Fig. 5.

Equation (5) is diagonalized together with an effective free-ion Hamiltonian of the form

$$H_{\text{free}}=\Sigma_{[SL]J}\Delta_{[SL]J}|[SL]J\rangle\langle[SL]J|, \tag{8}$$

where the sum on $[SL]J$ runs over the 15 lowest-energy $^{2S+1}L_J$ states (see Fig. 4 and Table V) of Dy^{3+} ($4f^9$). The quantities $\Delta_{[SL]J}$ are called centroids of the multiplet manifolds $^{2S+1}L_J$. By diagonalizing the sums of Eqs. (5) and (8), we include the major effects of J mixing between $^{2S+1}L_J$ states. By not diagonalizing the entire $4f^9$ electronic configuration, we conclude there are truncation errors in our results which can effect the calculated energy levels of the quartet states $^4F(3)_{9/2}$, $^4I(3)_{15/2}$, and $^4G(4)_{11/2}$. However, in the electron-hole symmetric $Sm^{3+}(4f^5)$ ion, the comparable electronic configuration, a comparative study between energy levels obtained from the diagonalization of the entire configuration and the method described here indicates that the sextet $^{2S+1}L_J$ states are least affected.[64] We expect in Dy^{3+} calculations (Tables VI and VII) that the fitting of the sextet states will not be significantly improved by diagonalizing the entire configuration (J mixing is more important here), but that the calculated splitting of the $^4F(3)_{9/2}$, $^4I(3)_{15/2}$, and $^4G(4)_{11/2}$ manifolds could be somewhat im-

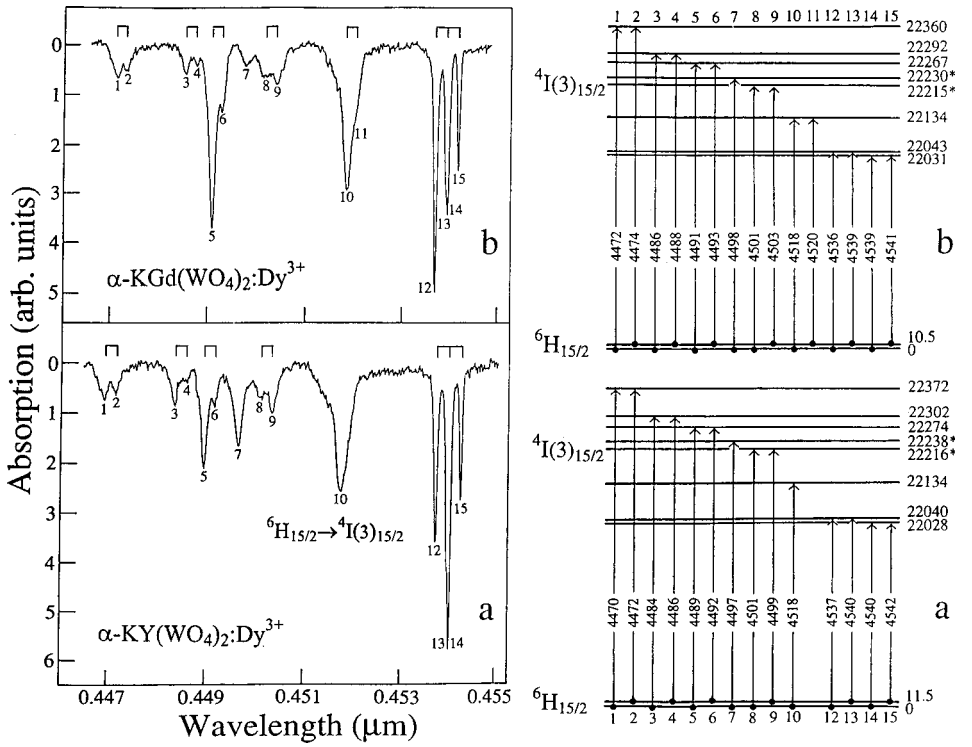

FIG. 14. Unpolarized absorption spectra ($^6H_{15/2}\rightarrow{}^4I(3)_{15/2}$ channel) and CF splitting schemes of the $^6H_{15/2}$ and $^4I(3)_{15/2}$ manifolds of Dy^{3+} ions in (a) α-$KY(WO_4)_2$ and (b) α-$KGd(WO_4)_2$ crystals at $\approx$15 K. Square brackets in the spectra indicate the energy-gap splitting between the two lowest-energy Stark levels of the ground state $^6H_{15/2}$. Other notations are the same as in Fig. 5.

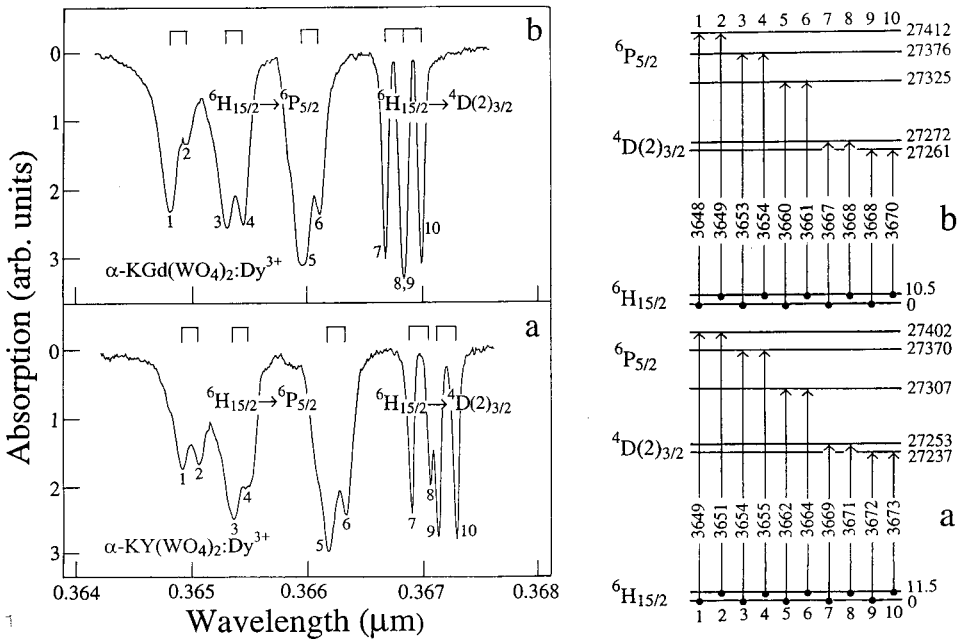

FIG. 15. Unpolarized absorption spectra ($^6H_{15/2}\rightarrow{}^4D(2)_{3/2}$ and $^6H_{15/2}\rightarrow{}^6P_{5/2}$ channels) and CF splitting schemes of the $^6H_{15/2}$, $^4D(2)_{3/2}$, and $^6P_{5/2}$ manifolds of Dy^{3+} ions in (a) α-$KY(WO_4)_2$ and (b) α-$KGd(WO_4)_2$ crystals at ≈15 K. Square brackets in the spectra indicate the energy-gap splitting between the two lowest-energy Stark levels of the ground state $^6H_{15/2}$. Other notations are the same as in Fig. 5.

proved by a full matrix diagonalization. Matrix elements of the crystal-field Hamiltonian [Eq. (7)] are obtained from wave functions associated with the intermediate-coupling diagonalization interactions of a free-ion Hamiltonian consisting of Coulombic, spin-orbit, and configuration interactions. Parameter values for the free-ion Hamiltonian are those obtained for Ln^{3+} ions in an aqueous solution.[65]

All experimental Stark levels of Dy^{3+} activators presented in Tables VI and VII are associated with the 15 $^{2S+1}L_J$ manifolds in α-$KY(WO_4)_2$ and α-$KGd(WO_4)_2$ tungstates. These 73 Stark levels were included in a least-squares-fitting analysis between the calculated and observed levels. The initial set of B_{nm} parameters were obtained from the calculated lattice-sum B_{nm}, and are listed in Table VIII. The final set obtained are listed there as well. For Dy^{3+} ions in α-$KY(WO_4)_2$, the rms deviation is 11 cm^{-1}; for Dy^{3+} in α-$KGd(WO_4)_2$, the rms deviation is 10 cm^{-1}. These values are comparable to the rms deviation obtained for Dy^{3+} in C_2 sites of Y_2O_3 (12 cm^{-1}).[66] Originally experimental levels in Table VI (levels 60–67) were reported as 22 027, 22 040, 22 147, 22 218, 22 239, 22 274, 22 302, and 22 374, and in Table VII (levels 60–70) as 22 031, 22 045, 22 133, 22 204, 22 267, 22 294, and 22 360 (all in cm^{-1}). These levels were used in the overall fitting of calculated-to-experimental levels described. Since those calculations were made, improved data were obtained for these levels that resulted in the minor

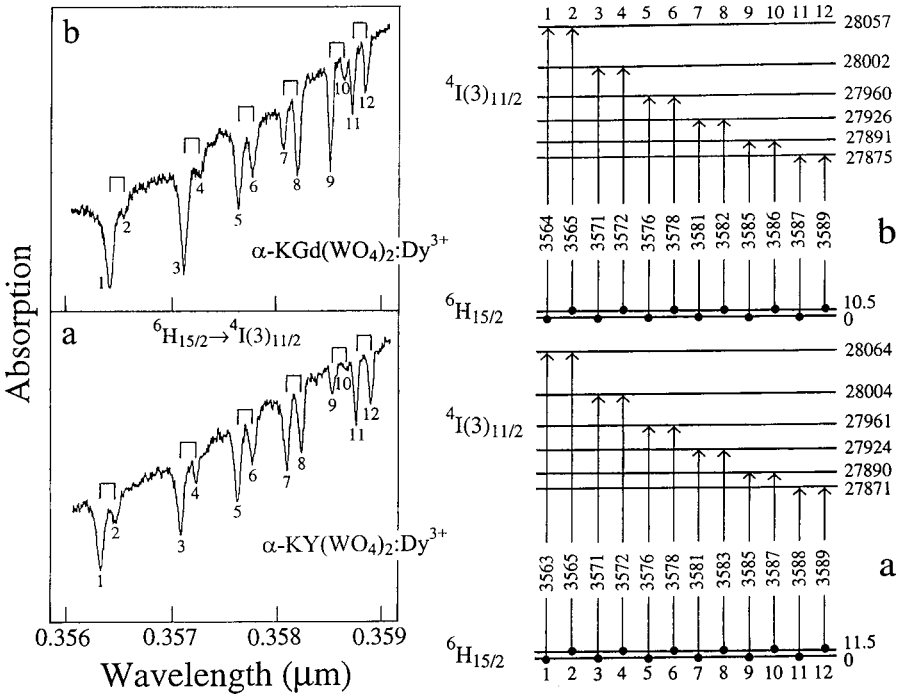

FIG. 16. Unpolarized absorption spectra ($^6H_{15/2}\rightarrow{}^4I(3)_{11/2}$ channel) and CF splitting schemes of the $^6H_{15/2}$ and $^4I(3)_{11/2}$ manifolds of Dy^{3+} ions in (a) α-$KY(WO_4)_2$ and (b) α-$KGd(WO_4)_2$ crystals at ≈15 K. Square brackets in the spectra indicate the energy-gap splitting between the two lowest-energy Stark levels of the ground state $^6H_{15/2}$. Other notations are the same as in Fig. 5.

TABLE V. Observed Stark levels of Dy^{3+} ions in monoclinic α-$KY(WO_4)_2$ and α-$KGd(WO_4)_2$ tungstates at ≈15 K.

$^{2S+1}L_J$ manifold	Stark level energy[a] (cm^{-1})	Number of levels		ΔE[b] (cm^{-1})
		Theor.	Expt.	
	α-$KY(WO_4)_2$			
$^6H_{15/2}$	0, 11.5, 137, 198, 273, 326, 420, 512	8	8	512
$^6H_{13/2}$	3565, 3584, 3630, 3687, 3724, 3788, 3865	7	7	300
$^6H_{11/2}$	5901, 5929, 5965, 6019, 6080, 6130	6	6	229
$[^6H_{9/2}+^6F_{11/2}]$	7696, 7721, 7747, 7758, 7814, 7843, 7868, 7911, 7944, 8006, 8032	11	11	(336)
$[^6F_{9/2}+^6H_{7/2}]$	9054, 9098, 9150, 9160, 9199, 9260, 9293, 9360, 9392	9	9	(338)
$^6H_{5/2}$	10 226, 10 290, 10 475*	3	3	249*
$^6F_{7/2}$	11 037, 11 064, 1119, 11 151	4	4	114
$^6F_{5/2}$	12 429, 12 478, 12 538	3	3	109
$^6F_{3/2}$	13 268, 13 289	2	2	21
$^6F_{1/2}$	13 824	1	1	-
$^4F(3)_{9/2}$	20 997, 21 047, 21 135, 21 278, 21 338	5	5	341
$^4I(3)_{15/2}$	22 028, 22 040, 22 134, 22 216, 22 238, 22 274, 22 302, 22 372	8	8	344
$^4G(4)_{11/2}$	23 400, 23 438, 23 470, 23 506, 23 560, 23 603	6	6	203
$[^4M_{21/2}+^4K(1)_{17/2}+$ $+^4I(3)_{13/2}+^4F(3)_{7/2}]$	24 858*, 24 949*, 24 986, 25 023, 25 122, 25 207, 25 238, 25 333, 25 344, 25 567, 25 589, 25 620, 25 631, 25 665, 25 726, 25 767, 25 809, 25 830, 25 850*, 25 882, 25 939*, 25 959*, 25 997*	31	23	(1139*)
$^4M_{19/2}$	26 300*, 26 312*, 26 424*, 26 384*, 26 452	10	5	152*
$^4D(2)_{3/2}$	27 237, 27 253	2	2	16
$^6P_{5/2}$	27 307, 27 370, 27 402	3	3	95
$^4I(3)_{11/2}$	27 871, 27 890, 27 924, 27 961, 28 004, 28 064	6	6	193
$[^6P_{7/2}+^4M_{15/2}]$	28 248, 28 342, 28 395, 28 418, 28 481*, 28 493, 28 503, 28 573, 28 591, 28 643*, 28 713*	12	11	(465*)
	α-$KGd(WO_4)_2$			
$^6H_{15/2}$	0, 10.5, 129, 190, 260, 308, 398, 487	8	8	487
$^6H_{13/2}$	3556, 3574, 3619, 3673, 3709, 3770, 3840	7	7	284
$^6H_{11/2}$	5896, 5928, 5960, 6010, 6066, 6112	6	6	216
$[^6H_{9/2}+^6F_{11/2}]$	7696, 7720, 7747, 7755, 7812, 7840, 7859, 7907, 7935, 7993, 8017	11	11	(321)
$[^6F_{9/2}+^6H_{7/2}]$	9052, 9094, 9143, 9151, 9189, 9251, 9295, 9345, 9378	9	9	(326)
$^6H_{5/2}$	10 222, 10 285, 10 460*	3	3	238*
$^6F_{7/2}$	11 032, 11 056, 11 115, 11 145	4	4	113
$^6F_{5/2}$	12 424, 12 471, 12 530	3	3	106
$^6F_{3/2}$	13 263, 13 280	2	2	17
$^6F_{1/2}$	13 817	1	1	-
$^4F(3)_{9/2}$	20 998, 21 048, 21 134, 21 275, 21 327	5	5	329
$^4I(3)_{15/2}$	22 031, 22 043, 22 134, 22 215, 22 230, 22 267, 22 292, 22 360	8	8	329
$^4G(4)_{11/2}$	23 402, 23 440, 23 469, 23 502, 23 553, 23 595	6	6	193
$[^4M_{21/2}+^4K(1)_{17/2}+$ $+^4I(3)_{13/2}+^4F(3)_{7/2}]$	24 861*, 24 865*, 24 955*, 24 993, 25 024, 25 121, 25 177*, 25 234, 25 329*, 25 342, 25 568, 25 591, 25 625, 25 633, 25 662, 25 728, 25 767, 25 806, 25 827, 25 846, 25 880, 25 930*, 25 950*, 26 001	31	24	(1140*)

TABLE V. (*Continued*.)

$^{2S+1}L_J$ manifold	Stark level energy[a] (cm^{-1})	Number of levels		ΔE[b] (cm^{-1})
		Theor.	Expt.	
$^4M_{19/2}$	26 296*, 26 310*, 26 319**, 26 334, 26 370*, 26 387, 26 412, 26 441, 26 460	10	9	164*
$^4D(2)_{3/2}$	27 261, 27 272	2	2	11
$^6P_{5/2}$	27 325, 27 376, 27 412	3	3	87
$^4I(3)_{11/2}$	27 875, 27 891, 27 926, 27 960, 28 002, 28 057	6	6	182
$[^6P_{7/2}+^4M_{15/2}]$	28 266, 28 356, 28 404, 28 427, 28 496, 28 505, 28 573, 28 640, 28 700*, 28 772*	12	10	(506*)

[a]The measurement accuracy is ± 0.0002 cm^{-1}. The Stark-level energies and total splitting ΔE of the $^{2S+1}L_J$ manifolds, denoted by an asterisk, require more accurate definition.

[b]If the Stark levels of the near-lying or overlapping $^{2S+1}L_J$ manifolds are not identified, their total splitting is given in brackets.

changes reported in Tables VI and VII. These changes are within the error analysis reported in terms of the rms deviation, and therefore it was not necessary to recalculate the entire energy level matrix.

Using the CF strength parameter

$$s=\{\tfrac{1}{3}\Sigma_n(1/(2n+1)[B_{n0}^2+2\Sigma_{m>0}(\mathrm{Re}\,B_{nm}^2+\mathrm{Im}\,B_{nm}^2)]\}^{1/2}, \tag{9}$$

where Re refers to the real CF parameter and Im to the imaginary CF parameter, we can express a quantitative measure of the strength of the CF interaction between the Dy^{3+} activator ion and the host lattice. We conclude that the crystal field is approximately twice as strong in our investigated monoclinic tungstates and in Y_2O_3, as reported in LaF_3 crystals. This conclusion is also supported by examining the magnitudes of the experimental CF splitting of the same levels in different host crystals. If the relative goodness of fit is the ratio of Q (rms) to s, then the calculations for Dy^{3+} ions in the monoclinic tungstates provide better agreement than those obtained earlier for Dy^{3+} in trigonal LaF_3 crystals[64] and cubic Y_2O_3 (C_2 sites) crystals.[66]

V. RADIATIVE INTERMANIFOLD TRANSITION INTENSITIES CALCULATION

Radiative transition calculations based on the well-known Judd-Ofelt (*J-O*) approach for weak inter-configuration interactions[67,68] have become widely used for predicting the SE potential of Ln^{3+} ions in crystals—in particular, such important parameters as intermanifold and inter-Stark luminescence branching ratios, as well as radiative lifetimes (see, for example, Ref. 18 and 69, and references therein). Chronologically, this method was initially used for the investigation of inter-Stark transition intensities (Eu^{3+} and Tm^{3+}).[70,71] Thereupon, during the next decade, this procedure was actively developed and successfully applied to luminescence intermanifold transition probability calculations of lasing Ln^{3+} activators in different fluoride and oxide crystal hosts having ordered and disordered structures.[72–80] It is well known that for Ln^{3+} ions the intermanifold line strength of magnetic-dipole (md) transitions is much less than the line strength of electric-dipole (ed) transitions ($s_{JJ'}^{md} \ll s_{JJ'}^{ed}$).[65,81] Therefore, in radiative intensity calculations the ed approximation is commonly used, and md transitions are only taken into account if required. It is desirable on occasion to place emphasis also on hypersensitive transitions.[69,82,83] In such studies of Dy^{3+}-doped compounds, all these factors should be kept in mind. Up to now, to the best of our knowledge the above-mentioned method has been employed for a luminescence intensity determination for only a very few laser crystals doped with Dy^{3+} ions (β-$BaYb_2F_8$, KPb_2Cl_5, and $CaGa_2S_4$).[84,85] All these materials are low-energy phonon crystals and exhibit SE generation around $\approx$2.4 μm ($[^6H_{9/2}+^6F_{11/2}]\rightarrow{}^6H_{13/2}$), $\approx$3 μm ($^6H_{13/2}\rightarrow{}^6H_{15/2}$), and $\approx$4.35 μm ($^6H_{13/2}\rightarrow{}^6H_{11/2}$) spectral regions.[84,86] In this paper we are interested in the intensity of luminescence intermanifold transitions which originate from the $^4F(3)_{9/2}$ state, and which help in the characterization of visible SE channels[16] of Dy^{3+} ions in monoclinic α-$KY(WO_4)_2$ and α-$KGd(WO_4)_2$ crystals. Since the luminescence properties of these laser tungstates are similar,[87] we determined the intermanifold radiative intensity characteristics only for an α-$KGd(WO_4)_2$:Dy^{3+} crystal. This calculation, as noted above in Sec. I, was carried out by the usual method on the basis of the *J-O* approach,[67,68] as well as by a method which takes into account the influence of excited electronic configurations.[88]

As a basis for this analysis, the experimental data for the integrated absorption coefficients $[\int k_{JJ'}(\lambda)d\lambda]$ are given for the 13 intermanifold $J(^6H_{15/2})\rightarrow J'$ band-areas for which we have measured values from the survey spectrum shown in Fig. 17. Two absorption channels $^6H_{15/2}\rightarrow{}^6H_{5/2}$ and $^6H_{15/2}\rightarrow{}^6H_{13/2}$ are not included in our calculation fit for different reasons. The integrated absorption coefficient for the first channel is very weak, and for the second intermanifold transition the band character contains a very large md component. The survey spectrum was obtained using samples con-

TABLE VI. Crystal-field splitting of Dy^{3+} energy levels in α-$KY(WO_4)_2$ single crystal.

$^{2S+1}L_J$ manifold[a]	Stark level[b]	E_{expt}[c] (cm^{-1})	E_{calc}[d] (cm^{-1})	Percent free ion manifolds[e]
$^6H_{15/2}$ (246)	1	0	3	99.8 $^6H_{15/2}$+0.10 $^6F_{11/2}$+0.05 $^6H_{13/2}$
	2	11.5	25	99.8 $^6H_{15/2}$+0.12 $^6F_{11/2}$+0.04 $^6H_{13/2}$
	3	137	139	99.7 $^6H_{15/2}$+0.20 $^6H_{13/2}$+0.02 $^6F_{11/2}$
	4	198	193	99.7 $^6H_{15/2}$+0.22 $^6H_{13/2}$+0.04 $^6F_{11/2}$
	5	273	280	99.7 $^6H_{15/2}$+0.20 $^6H_{13/2}$+0.03 $^6F_{11/2}$
	6	326	330	99.9 $^6H_{15/2}$+0.06 $^6H_{13/2}$+0.02 $^6H_{11/2}$
	7	420	406	99.8 $^6H_{15/2}$+0.12 $^6H_{13/2}$+0.04 $^6F_{9/2}$
	8	512	502	99.9 $^6H_{15/2}$+0.06 $^6H_{13/2}$+0.03 $^6F_{11/2}$
$^6H_{13/2}$ (3704)	9	3565	3563	99.5 $^6H_{13/2}$+0.23 $^6F_{11/2}$+0.13 $^6H_{15/2}$
	10	3584	3585	99.5 $^6H_{13/2}$+0.17 $^6H_{15/2}$+0.14 $^6F_{11/2}$
	11	3630	3641	99.2 $^6H_{13/2}$+0.55 $^6H_{11/2}$+0.11 $^6F_{11/2}$
	12	3687	3688	99.3 $^6H_{13/2}$+0.38 $^6H_{11/2}$+0.18 $^6H_{15/2}$
	13	3724	3717	99.4 $^6H_{13/2}$+0.27 $^6H_{11/2}$+0.15 $^6H_{15/2}$
	14	3788	3781	99.3 $^6H_{13/2}$+0.31 $^6H_{11/2}$+0.19 $^6H_{15/2}$
	15	3865	3869	99.6 $^6H_{13/2}$+0.18 $^6H_{11/2}$+0.08 $^6H_{15/2}$
$^6H_{11/2}$ (6016)	16	5901	5904	99.0 $^6H_{11/2}$+0.53 $^6H_{13/2}$+0.26 $^6F_{11/2}$
	17	5929	5926	98.8 $^6H_{11/2}$+0.32 $^6H_{9/2}$+0.31 $^6F_{11/2}$
	18	5965	5975	98.7 $^6H_{11/2}$+0.35 $^6H_{13/2}$+0.34 $^6F_{11/2}$
	19	6019	6012	98.7 $^6H_{11/2}$+0.35 $^6H_{13/2}$+0.33 $^6H_{11/2}$
	20	6080	6073	98.8 $^6H_{11/2}$+0.37 $^6H_{9/2}$+0.36 $^6H_{13/2}$
	21	6130	6134	99.0 $^6H_{11/2}$+0.26 $^6F_{11/2}$+0.24 $^6H_{9/2}$
$^6F_{11/2}$ (7830)	22	7696	7673	62.0 $^6H_{9/2}$+37.1 $^6F_{11/2}$+0.38 $^6H_{11/2}$
	23	7721	7713	72.9 $^6F_{11/2}$+26.2 $^6H_{9/2}$+0.42 $^6H_{11/2}$
$^6H_{9/2}$ (7877)	24	7747	7753	83.9 $^6F_{11/2}$+15.4 $^6H_{9/2}$+0.29 $^6H_{11/2}$
	25	7758	7779	52.5 $^6F_{11/2}$+46.4 $^6H_{9/2}$+0.31 $^6F_{9/2}$
	26	7814	7804	61.9 $^6F_{11/2}$+37.0 $^6H_{9/2}$+0.37 $^6F_{9/2}$
	27	7843	7850	56.5 $^6H_{9/2}$+42.1 $^6F_{11/2}$+0.77 $^6F_{9/2}$
	28	7868	7874	55.2 $^6F_{11/2}$+43.5 $^6H_{9/2}$+0.55 $^6F_{9/2}$
	29	7911	7915	66.8 $^6H_{9/2}$+31.5 $^6F_{11/2}$+0.62 $^6H_{7/2}$
	30	7944	7927	59.5 $^6F_{11/2}$+39.5 $^6H_{9/2}$+0.39 $^6F_{9/2}$
	31	8006	8013	56.3 $^6H_{9/2}$+41.8 $^6F_{11/2}$+0.59 $^6H_{7/2}$
	32	8032	8039	57.9 $^6F_{11/2}$+40.9 $^6H_{9/2}$+0.60 $^6H_{11/2}$
$^6F_{9/2}$ (9169)	33	9054	9053	54.1 $^6F_{9/2}$+44.2 $^6H_{7/2}$+0.86 $^6H_{9/2}$
	34	9098	9086	59.8 $^6F_{9/2}$+38.6 $^6H_{7/2}$+0.85 $^6H_{5/2}$
$^6H_{7/2}$ (9271)	35	9150	9149	74.3 $^6F_{9/2}$+24.5 $^6H_{7/2}$+0.51 $^6H_{9/2}$
	36	9160	9169	85.2 $^6F_{9/2}$+13.6 $^6H_{7/2}$+0.78 $^6H_{9/2}$
	37	9199	9197	85.8 $^6F_{9/2}$+12.9 $^6H_{7/2}$+0.75 $^6H_{9/2}$
	38	9260	9260	53.1 $^6F_{9/2}$+44.8 $^6H_{7/2}$+0.75 $^6H_{5/2}$
	39	9293	9304	59.5 $^6H_{7/2}$+38.4 $^6F_{9/2}$+0.78 $^6H_{9/2}$
	40	9360	9352	72.7 $^6H_{7/2}$+44.8 $^6F_{9/2}$+1.32 $^6H_{5/2}$
	41	9392	9396	78.3 $^6H_{7/2}$+18.3 $^6F_{9/2}$+1.82 $^6H_{5/2}$
$^6H_{5/2}$ (10 331)	42	10 226	10 226	94.8 $^6H_{5/2}$+2.73 $^6H_{7/2}$+1.43 $^6F_{7/2}$
	43	10 290	10 289	94.9 $^6H_{5/2}$+2.47 $^6F_{7/2}$+1.68 $^6H_{7/2}$
	44	10 475	10 475	96.0 $^6H_{5/2}$+2.27 $^6F_{7/2}$+0.74 $^6H_{7/2}$
$^6F_{7/2}$ (11 064)	45	11 037	11 040	97.7 $^6F_{7/2}$+1.23 $^6H_{5/2}$+0.62 $^6H_{7/2}$
	46	11 064	11 071	98.8 $^6F_{7/2}$+0.55 $^6H_{5/2}$+0.22 $^6H_{9/2}$
	47	11 119	11 105	97.8 $^6F_{7/2}$+1.54 $^6H_{5/2}$+0.16 $^6H_{7/2}$
	48	11 151	11 156	96.4 $^6F_{7/2}$+2.61 $^6H_{5/2}$+0.71 $^6H_{7/2}$

TABLE VI. (*Continued*.)

$^{2S+1}L_J$ manifold[a]	Stark level[b]	E_{expt}[c] (cm^{-1})	E_{calc}[d] (cm^{-1})	Percent free ion manifolds[e]
$^6F_{5/2}$ (12 464)	49	12 429	12 446	98.6 $^6F_{5/2}$+0.82 $^6F_{3/2}$+0.30 $^6H_{5/2}$
	50	12 478	12 465	99.3 $^6F_{5/2}$+0.17 $^6F_{3/2}$+0.15 $^6H_{7/2}$
	51	12 538	12 534	99.0 $^6F_{5/2}$+0.66 $^6F_{3/2}$+0.30 $^6H_{5/2}$
$^6F_{3/2}$ (13 258)	52	13 268	13 267	99.0 $^6F_{3/2}$+0.50 $^6F_{1/2}$+0.11 $^6H_{7/2}$
	53	13 289	13 289	98.6 $^6F_{3/2}$+0.86 $^6F_{5/2}$+0.29 $^6H_{7/2}$
$^6F_{1/2}$ (13 803)	54	13 824	13 824	99.0 $^6F_{1/2}$+0.54 $^6F_{3/2}$+0.13 $^6H_{7/2}$
$^4F(3)_{9/2}$ (21 184)	55	20 997	21 023	97.6 $^4F(3)_{9/2}$+2.23 $^4I(3)_{15/2}$+0.15 $^4G(4)_{11/2}$
	56	21 047	21 066	97.6 $^4F(3)_{9/2}$+2.33 $^4I(3)_{15/2}$+0.10 $^4G(4)_{11/2}$
	57	21 135	21 145	98.3 $^4F(3)_{9/2}$+1.34 $^4I(3)_{15/2}$+0.36 $^4G(4)_{11/2}$
	58	21 278	21 240	98.2 $^4F(3)_{9/2}$+1.42 $^4I(3)_{15/2}$+0.36 $^4G(4)_{11/2}$
	59	21 338	21 321	97.4 $^4F(3)_{9/2}$+2.18 $^4I(3)_{15/2}$+0.41 $^4G(4)_{11/2}$
$^4I(3)_{15/2}$ (22 195)	60	22 028	22 011	99.0 $^4I(3)_{15/2}$+0.80 $^4F(3)_{9/2}$+0.25 $^4G(4)_{11/2}$
	61	22 040	22 038	98.9 $^4I(3)_{15/2}$+0.93 $^4F(3)_{9/2}$+0.18 $^4G(4)_{11/2}$
	62	22 134	22 128	97.4 $^4I(3)_{15/2}$+2.32 $^4F(3)_{9/2}$+0.25 $^4G(4)_{11/2}$
	63	22 216	22 207	97.9 $^4I(3)_{15/2}$+1.69 $^4F(3)_{9/2}$+0.40 $^4G(4)_{11/2}$
	64	22 238	22 241	97.9 $^4I(3)_{15/2}$+1.56 $^4F(3)_{9/2}$+0.51 $^4G(4)_{11/2}$
	65	22 274	22 294	99.1 $^4I(3)_{15/2}$+0.62 $^4G(4)_{11/2}$+0.33 $^4F(3)_{9/2}$
	66	22 302	22 316	98.2 $^4I(3)_{15/2}$+1.32 $^4F(3)_{9/2}$+0.48 $^4G(4)_{11/2}$
	67	22 372	22 387	99.1 $^4I(3)_{15/2}$+0.72 $^4F(3)_{9/2}$+0.20 $^4G(4)_{11/2}$
$^4G(4)_{11/2}$ (23 485)	68	23 400	23 382	99.2 $^4G(4)_{11/2}$+0.73 $^4I(3)_{15/2}$+0.04 $^4F(3)_{9/2}$
	69	23 438	23 423	99.3 $^4G(4)_{11/2}$+0.70 $^4I(3)_{15/2}$+0.04 $^4F(3)_{9/2}$
	70	23 470	23 489	99.4 $^4G(4)_{11/2}$+0.32 $^4F(3)_{9/2}$+0.31 $^4I(3)_{15/2}$
	71	23 506	23 514	99.1 $^4G(4)_{11/2}$+0.51 $^4F(3)_{9/2}$+0.44 $^4I(3)_{15/2}$
	72	23 560	23 563	99.2 $^4G(4)_{11/2}$+0.56 $^4I(3)_{15/2}$+0.25 $^4F(3)_{9/2}$
	73	23 603	23 605	99.6 $^4G(4)_{11/2}$+0.35 $^4I(3)_{15/2}$+0.04 $^4F(3)_{9/2}$

[a]Multiplet manifolds of Dy^{3+} ions ($4f^9$), $^{2S+1}L_J$; the number in parentheses is the calculated centroid for the manifold.

[b]All Stark levels have the same symmetry label ($\mu=\pm 1/2$); the point group symmetry for Dy^{3+} ions is C_2 in sites of α-$KY(WO_4)_2$ crystal (see Table II).

[c]All levels observed at ≈15 K are used in a least-squares fitting to the calculated levels. Initial CF parameters, B_{nm} were obtained from lattice-sum calculations.

[d]Seventy-three calculated to observed Stark levels. The rms deviation is 11 cm^{-1}. B_{nm} initial and final values are given in Table VIII.

[e]Percent of free-ion mixing of $^{2S+1}L_J$ manifolds of Dy^{3+} ions.

structed as sandwiches composed of three equal thicknesses and Dy^{3+}-ion concentration plane-parallel plates oriented along the *a*, *b*, and *c* axes. In the approximation involving a weak interconfiguration interaction, we assume the energy separations of an excited configuration of opposite party to be identical for each manifold included in the transition.[67,68] In this case, the line strength of an intermanifold $J\rightarrow J'$ transitions is given by the expression

$$S^{ed}_{JJ'}=e^2\Sigma_{t=2,4,6}\Omega_t|\langle 4f^N[SL]J\|U^{(t)}\|4f^N[S'L']J'\rangle|^2, \quad (10)$$

where Ω_t are the intensity parameters which reflect the fundamental coupling of the probabilities of the quantum ed transitions in absorption and luminescence, and $\langle\cdots\|U^{(t)}\|\cdots\rangle$ are the reduced matrix elements of a unit tensor operator $U^{(t)}$ of rank *t*.

The approximation of weak interconfiguration intertaction will be correct only if the energy of the excited configuration is significantly larger than the manifold energy of the ground-state configuration. Actually, the manifold energies of Ln^{3+} ions have the same order of magnitude as the energy of excited configurations. Thus the conditions for the applicability of weak interconfiguration interaction are seldom realized, and the use of Eq. (10) should meet with inconsistency. The energy differences will vary between excited configurations and higher-lying manifolds of the $4f^N$ configuration relative to the lower-lying manifolds. This effect was taken into account in Ref. 88, where the energy depen-

TABLE VII. Crystal-field splitting of Dy^{3+} energy levels in α-$KGd(WO_4)_2$ single crystal.

$^{2S+1}L_J$ manifold[a]	Stark level[b]	E_{expt}[c] (cm^{-1})	E_{calc}[d] (cm^{-1})	Percent free ion manifolds[e]
$^6H_{15/2}$	1	0	−3	99.8 $^6H_{15/2}$+0.11 $^6F_{11/2}$+0.05 $^6H_{13/2}$
(234)	2	10.5	17	99.8 $^6H_{15/2}$+0.13 $^6F_{11/2}$+0.04 $^6H_{13/2}$
	3	129	127	99.8 $^6H_{15/2}$+0.19 $^6H_{13/2}$+0.02 $^6F_{11/2}$
	4	190	175	99.7 $^6H_{15/2}$+0.23 $^6H_{13/2}$+0.04 $^6F_{11/2}$
	5	260	268	99.7 $^6H_{15/2}$+0.23 $^6H_{13/2}$+0.03 $^6F_{9/2}$
	6	308	321	99.9 $^6H_{15/2}$+0.04 $^6H_{13/2}$+0.01 $^6H_{11/2}$
	7	398	393	99.8 $^6H_{15/2}$+0.13 $^6H_{13/2}$+0.04 $^6F_{9/2}$
	8	487	486	99.9 $^6H_{15/2}$+0.05 $^6H_{13/2}$+0.03 $^6F_{11/2}$
$^6H_{13/2}$	9	3556	3552	99.3 $^6H_{13/2}$+0.33 $^6H_{11/2}$+0.15 $^6F_{11/2}$
(3690)	10	3574	3579	99.5 $^6H_{15/2}$+0.16 $^6H_{15/2}$+0.11 $^6F_{11/2}$
	11	3619	3630	99.2 $^6H_{13/2}$+0.52 $^6H_{11/2}$+0.10 $^6F_{11/2}$
	12	3673	3678	99.3 $^6H_{13/2}$+0.36 $^6H_{11/2}$+0.17 $^6H_{15/2}$
	13	3709	3700	99.4 $^6H_{13/2}$+0.29 $^6H_{11/2}$+0.16 $^6H_{15/2}$
	14	3770	3763	99.3 $^6H_{13/2}$+0.33 $^6H_{11/2}$+0.20 $^6H_{15/2}$
	15	3840	3842	99.5 $^6H_{13/2}$+0.19 $^6H_{11/2}$+0.08 $^6H_{15/2}$
$^6H_{11/2}$	16	5896	5896	98.9 $^6H_{11/2}$+0.63 $^6H_{13/2}$+0.28 $^6F_{11/2}$
(6007)	17	5928	5928	98.9 $^6H_{11/2}$+0.35 $^6H_{9/2}$+0.25 $^6F_{11/2}$
	18	5960	5969	98.7 $^6H_{11/2}$+0.43 $^6F_{9/2}$+0.33 $^6F_{11/2}$
	19	6010	6005	98.7 $^6H_{11/2}$+0.43 $^6H_{13/2}$+0.33 $^6F_{11/2}$
	20	6066	6062	98.8 $^6H_{11/2}$+0.40 $^6H_{13/2}$+0.35 $^6H_{9/2}$
	21	6112	6111	98.9 $^6H_{11/2}$+0.28 $^6H_{9/2}$+0.25 $^6H_{13/2}$
$^6F_{11/2}$	22	7696	7668	55.5 $^6H_{9/2}$+43.5 $^6F_{11/2}$+0.50 $^6H_{11/2}$
(7822)	23	7720	7712	77.6 $^6F_{11/2}$+21.5 $^6H_{9/2}$+0.37 $^6H_{11/2}$
$^6H_{9/2}$	24	7747	7748	84.7 $^6F_{11/2}$+14.6 $^6H_{9/2}$+0.28 $^6H_{11/2}$
(7877)	25	7755	7770	65.2 $^6F_{11/2}$+34.0 $^6H_{9/2}$+0.24 $^6H_{11/2}$
	26	7812	7806	53.0 $^6H_{9/2}$+45.7 $^6F_{11/2}$+0.53 $^6F_{9/2}$
	27	7840	7849	67.6 $^6H_{9/2}$+30.7 $^6F_{11/2}$+0.91 $^6F_{9/2}$
	28	7859	7874	63.5 $^6F_{11/2}$+35.4 $^6H_{9/2}$+0.54 $^6F_{9/2}$
	29	7907	7908	69.7 $^6H_{9/2}$+28.5 $^6F_{11/2}$+0.61 $^6F_{9/2}$
	30	7935	7917	57.7 $^6F_{11/2}$+41.2 $^6H_{9/2}$+0.53 $^6F_{9/2}$
	31	7993	8003	69.5 $^6H_{9/2}$+28.7 $^6F_{11/2}$+0.59 $^6F_{7/2}$
	32	8017	8026	70.5 $^6F_{11/2}$+28.1 $^6H_{9/2}$+0.66 $^6H_{11/2}$
$^6F_{9/2}$	33	9052	9050	58.4 $^6F_{9/2}$+40.0 $^6H_{7/2}$+0.94 $^6H_{9/2}$
(9158)	34	9094	9086	64.8 $^6F_{9/2}$+33.7 $^6H_{7/2}$+0.76 $^6H_{5/2}$
$^6H_{7/2}$	35	9143	9143	75.3 $^6F_{9/2}$+23.4 $^6H_{7/2}$+0.66 $^6H_{9/2}$
(9268)	36	9151	9161	83.0 $^6F_{9/2}$+15.7 $^6H_{7/2}$+0.88 $^6H_{9/2}$
	37	9189	9186	85.5 $^6F_{9/2}$+12.9 $^6H_{7/2}$+0.94 $^6H_{9/2}$
	38	9251	9252	49.7 $^6H_{7/2}$+48.3 $^6F_{9/2}$+0.65 $^6H_{5/2}$
	39	9295	9300	63.5 $^6H_{7/2}$+34.4 $^6F_{9/2}$+0.71 $^6H_{9/2}$
	40	9345	9341	72.3 $^6H_{7/2}$+25.1 $^6F_{9/2}$+1.14 $^6H_{5/2}$
	41	9378	9381	77.5 $^6H_{7/2}$+18.7 $^6F_{9/2}$+2.14 $^6H_{5/2}$
$^6H_{5/2}$	42	10 222	10 224	94.6 $^6H_{5/2}$+3.04 $^6H_{7/2}$+1.29 $^6F_{7/2}$
(10 323)	43	10 285	10 280	95.2 $^6H_{5/2}$+ 2.34 $^6F_{7/2}$+ 1.57 $^6H_{7/2}$
	44	10 460	10 463	96.1 $^6H_{5/2}$+ 2.17 $^6F_{7/2}$+ 0.81 $^6H_{7/2}$
$^6F_{7/2}$	45	11 032	11 033	97.9 $^6F_{7/2}$+1.08 $^6H_{5/2}$+0.63 $^6H_{7/2}$
(11 059)	46	11 058	11 066	98.7 $^6F_{7/2}$+0.52 $^6H_{5/2}$+0.24 $^6H_{7/2}$
	47	11 115	11 096	97.7 $^6F_{7/2}$+1.64 $^6H_{5/2}$+0.18 $^6F_{5/2}$
	48	11 145	11 156	96.6 $^6F_{7/2}$+2.38 $^6H_{5/2}$+0.77 $^6H_{7/2}$

TABLE VII. (*Continued*.)

$^{2S+1}L_J$ manifold[a]	Stark level[b]	E_{expt}[c] (cm^{-1})	E_{calc}[d] (cm^{-1})	Percent free ion manifolds[e]
$^6F_{5/2}$	49	12 424	12 436	$98.5\ ^6F_{5/2}+0.94\ ^6F_{3/2}+0.28\ ^6H_{5/2}$
(12 457)	50	12 471	12 457	$99.3\ ^6F_{5/2}+0.14\ ^6H_{7/2}+0.13\ ^6F_{3/2}$
	51	12 530	12 531	$98.9\ ^6F_{5/2}+0.72\ ^6H_{5/2}+0.14\ ^6F_{7/2}$
$^6F_{3/2}$	52	13 263	13 262	$99.1\ ^6F_{3/2}+0.42\ ^6F_{1/2}+0.10\ ^6H_{5/2}$
(13 251)	53	13 280	13 283	$98.4\ ^6F_{3/2}+0.94\ ^6F_{5/2}+0.29\ ^6H_{5/2}$
$^6F_{1/2}$ (13 796)	54	13 817	13 817	$99.0\ ^6F_{1/2}+0.51\ ^6F_{3/2}+0.15\ ^6H_{7/2}$
$^4F(3)_{9/2}$	55	20 998	21 013	$97.4\ ^4F(3)_{9/2}+2.53\ ^4I(3)_{15/2}+0.11\ ^4G(4)_{11/2}$
(21 183)	56	21 048	21 057	$97.5\ ^4F(3)_{9/2}+2.42\ ^4I(3)_{15/2}+0.09\ ^4G(4)_{11/2}$
	57	21 134	21 152	$98.3\ ^4F(3)_{9/2}+1.40\ ^4I(3)_{15/2}+\ 0.31^4G(4)_{11/2}$
	58	21 275	21 264	$98.1\ ^4F(3)_{9/2}+1.55\ ^4I(3)_{15/2}+0.35\ ^4G(4)_{11/2}$
	59	21 327	21 314	$97.4\ ^4F(3)_{9/2}+2.21\ ^4I(3)_{15/2}+0.43\ ^4G(4)_{11/2}$
$^4I(3)_{15/2}$	60	22 031	22 023	$99.1\ ^4I(3)_{15/2}+0.65\ ^4F(3)_{9/2}+0.22\ ^4G(4)_{11/2}$
(22 204)	61	22 043	22 052	$98.9\ ^4I(3)_{15/2}+1.01\ ^4F(3)_{9/2}+0.10\ ^4G(4)_{11/2}$
	62	22 134	22 133	$97.3\ ^4I(3)_{15/2}+2.49\ ^4F(3)_{9/2}+0.18\ ^4G(4)_{11/2}$
	63	22 215	22 213	$97.6\ ^4I(3)_{15/2}+2.05\ ^4F(3)_{9/2}+0.33\ ^4G(4)_{11/2}$
	64	22 230	22 259	$97.8\ ^4I(3)_{15/2}+1.69\ ^4F(3)_{9/2}+0.49\ ^4G(4)_{11/2}$
	65	22 267	22 313	$99.3\ ^4I(3)_{15/2}+0.42\ ^4G(4)_{11/2}+0.25\ ^4F(3)_{9/2}$
	66	22 292	22 329	$98.2\ ^4I(3)_{15/2}+1.39\ ^4F(3)_{9/2}+0.45\ ^4G(4)_{11/2}$
	67	22 360	22 388	$99.0\ ^4I(3)_{15/2}+0.75\ ^4F(3)_{9/2}+0.27\ ^4G(4)_{11/2}$
$^4G(4)_{11/2}$	68	23 402	23 407	$99.4\ ^4G(4)_{11/2}+0.53\ ^4I(3)_{15/2}+0.04\ ^4F(3)_{9/2}$
(23 517)	69	23 440	23 440	$99.2\ ^4G(4)_{11/2}+0.74\ ^4I(3)_{15/2}+0.03\ ^4F(3)_{9/2}$
	70	23 469	23 469	$99.5\ ^4G(4)_{11/2}+0.27\ ^4F(3)_{9/2}+0.26\ ^4I(3)_{15/2}$
	71	23 502	23 500	$99.1\ ^4G(4)_{11/2}+0.51\ ^4F(3)_{9/2}+0.44\ ^4I(3)_{15/2}$
	72	23 552	23 540	$99.4\ ^4G(4)_{11/2}+0.04\ ^4I(3)_{15/2}+0.23\ ^4F(3)_{9/2}$
	73	23 595	23 590	$99.7\ ^4G(4)_{11/2}+0.27\ ^4I(3)_{15/2}+0.04\ ^4F(3)_{9/2}$

[a]Multiplet manifolds of Dy^{3+} ions ($4f^9$), $^{2S+1}L_J$; the number in parentheses is the calculated centroid for the manifold.

[b]All Stark levels have the same symmetry label ($\mu=\pm 1/2$); the point group symmetry for Dy^{3+} ions is C_2 in sites of α-$KGd(WO_4)_2$ crystal (see Table II).

[c]All observed levels at ≈15 K are used in a least-squares fitting to the calculated levels. Initial CF parameters B_{nm} were obtained from lattice-sum calculations.

[d]Seventy-three calculated to observed Stark levels. The rms deviation is 10 cm^{-1}. B_{nm} initial and final values are given in Table VIII.

[e]Percent free-ion mixing of $^{2S+1}L_J$ manifolds of Dy^{3+} ions.

dent expression for the line strengths was given as

$$S^{ed}_{JJ'}=e^2\Sigma_{t=2,4,6}\underbrace{\Omega_t[1+2R_t(E_J+E_{J'}-2E^0_f)]}_{\Omega^{\sim}_t}\times|\langle 4f^N[SL]J\|U^{(t)}\|4f^N[S'L']J'\rangle|^2+\text{terms of the odd rank.} \quad (11)$$

Equation (11) was obtained through an approximation if an intermediate interconfiguration interaction applies. Here $\Omega^{\sim}_t$ are the intensity parameters that depend linearly on manifold energy E_J and $E_{J'}$, E^0_f is the energy of the gravity center of the $4f^N$ configuration, and R_t is the additional parameter with $t=2,4,6$. The excited configurations with transfer of an electron from a ligand to $4f^N$-shell and opposite party configurations give comparable contributions to $\Omega^{\sim}_t$ and R_t. Therefore, values of R_2, R_4, and R_6 and Ω_2, Ω_4, and Ω_6 can essentially differ from each other. Only in those rare cases, when only one of the opposite party configurations gives the decisive contribution, can the following simple relation be obtained:

$$\alpha=R_2=R_4=R_6=1/2\Delta. \quad (12)$$

In Eq. (12), Δ is the energy of the excited configuration. Only in these cases is it possible to use the relation (12) for a determination of the number of parameters in Eq. (11).

TABLE VIII. Crystal-field parameters in units of cm^{-1}.

$P_{n,m}$ [a]	A_{nm} [b]	B_{nmi} [c]	$B_{nmf,A}$ [d]	$B_{nmf,B}$ [e]
2, 0	−4039	−679	−601	−544
2, 2	−511	−86	−16	−47.9
4, 0	−382	−166	−188	−245
4, 2	−1394	−605	−583	−638
4, 2 Im	507	220	271	258
4, 4	−1944	−844	−869	−900
4, 4 Im	548	238	243	259
6, 0	−79.9	−84.8	−41.6	−7.55
6, 2	−179	−190	−179	−116
6, 2 Im	−169	−179	−405	−343
6, 4	86.6	91.9	71.8	75
6, 4 Im	−184	−195	−183	−200
6, 6	159	169	−5.69	43.7
6, 6 Im	17.4	18.5	40.2	61.6

[a]First number represents, *n*; second number, *m* in parameter terms.
[b]Lattice-sum CF components [Eq. (3)].
[c]CF parameters obtained from three-parameter theory; $B_{nm}=\rho_n A_{nm}$ [Eq. (4)]; initial parameters used in calculations.
[d]Final set of B_{nm} for Dy^{3+} in α-$KY(WO_4)_2$; 73 levels where the rms deviation is 11 cm^{-1}; see Table VI for splitting results.
[e]Final set of B_{nm} for Dy^{3+} in α-$KGd(WO_4)_2$; 73 levels, where the rms deviation is 10 cm^{-1}; see Table VII for splitting results.

With a lowering of the excitation energy, as is the case for actinides and occasionally for some lanthanides, the influence of excited configurations on different manifolds within the ground-state configuration can be so significant that it should be taken into account even in the first order of the perturbation theory. In an approximation of such a strong interconfiguration interaction, the effective line strength operator was obtained in Refs. 89 and 90 as

$$S^{\mathrm{ed}}_{JJ'}=e^2\Sigma_{t=2,4,6}\underbrace{\Omega_t[\Delta/\Delta-E_J)+(\Delta/\Delta-E_{J'})]^2}_{\Omega_t^-}\times|\langle 4f^N[SL]J\|U^{(t)}\|4f^N[S'L']J'\rangle|^2+\text{terms of odd rank.} \tag{13}$$

In this approximation the intensity parameters Ω_t^- depend on the manifold energies under a more complicated law than a linear approximation. It is necessary to note that such a simple tensor operator form as given in Eq. (13), can be possible solely on the condition that only one excited configuration makes the main contribution to the transition line strength.[89]

Earlier several investigators were convinced,[88,89] that the influence of terms with tensors of odd ranks becomes noticeable in Eqs. (11) and (13) when only doubtful, large values of parameters are used to assign their amplitude. For these reasons we assume that the influence of the terms of odd rank are insignificant, so that it is possible to use simplified variants of Eqs. (11) and (13) for a description of the experimental data.[90–95]

For a theoretical analysis of our experimental data, we used the usual method mentioned above. The calculation was made on the basis of the *J-O* approach with the use of Eq. (10), as well as a calculation in the approximation of intermediate interconfiguration interaction, i.e., with use the Eq. (11). Intermanifold line strengths are related to the integrated absorption coefficient by the well-known relation

$$\int k_{JJ'}(\lambda)d\lambda=\{8\pi^3N_0\lambda^-_{JJ'}e^2/3ch(2J+1)\}\times\{(n^{-2}+2)^2/9n^-\}s^{\mathrm{ed}}_{JJ'}. \tag{14}$$

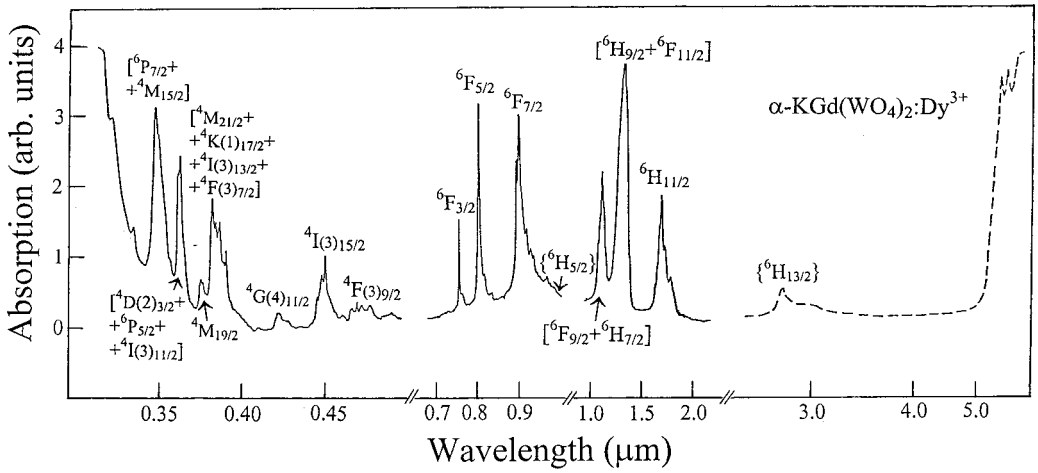

FIG. 17. Unpolarized survey absorption spectra of ≈1 at. % Dy^{3+}-ion-doped α-$KGd(WO_4)_2$ crystals at 300 K. The four parts of the spectrum were obtained with different thicknesses of the sample. The mid-IR of the spectrum (shown by dashed curve) was recorded with the spectrophotometer Specord 75IR. Also see the explanation in the text.

TABLE IX. Spectroscopic characteristics determining the intensity of absorption intermanifold $^6H_{15/2} \rightarrow J'$ band areas and intensity parameters for the Dy^{3+} ions in α-$KGd(WO_4)_2$ single crystal at 300 K.

Terminal manifold of absorption	$\lambda^-_{JJ'}$	n^-	Line strength (10^{-20} cm^2)		
$^6H_{15/2} \rightarrow J'$ channel	(μm)		$S^{ed}_{JJ'\,expt}$	$S^{ed}_{JJ'\,calc}$ [a]	$s^{ed}_{JJ'\,calc}$ [b]
$^6H_{11/2}$	≈1.68	≈2	2.39	2.717	2.740
$[^6H_{9/2}+{}^6F_{11/2}]$	≈1.29	2.01	17.9	17.892	17.995
$[^6F_{9/2}+{}^6H_{7/2}]$	≈1.1	2.02	2.56	3.286	2.891
$^6F_{7/2}$	≈0.9	2.03	2.58	1.849	2.243
$^6F_{5/2}$	≈1.68	2.04	0.9	0.711	1.052
$^6F_{3/2}$	≈0.8	2.04	0.21	0.126	0.195
$^4F(3)_{9/2}$	≈0.75	2.08	0.15	0.070	0.136
$^4I(3)_{15/2}$	≈0.45	2.09	0.26	0.241	0.408
$^4G(4)_{11/2}$	≈0.434	2.11	0.07	0.041	0.048
$[^4M_{21/2}+{}^4K(3)_{17/2}+{}^4I(3)_{13/2}+{}^4F(3)_{7/2}]$	≈0.426	2.11	1.47	0.811	1.313
$^4M_{19/2}$	≈0.387	2.13	0.17	0.248	0.563
$[^4D(2)_{3/2}+{}^6P_{5/2}+{}^4I(3)_{11/2}]$	≈0.366	2.14	0.76	0.322	0.849
$[^6P_{7/2}+{}^4M_{15/2}]$	≈0.352	2.14	2.09	1.621	2.155
rms				0.455	0.290
Parameters Ω_t (in 10^{-20} cm^2) and R_t (in 10^{-4} cm)					
Ω_2				15.347	9.878
Ω_4				3.053	14.631
Ω_6				2.006	19.966
R_2					−0.030
R_4					0.039
R_6					0.039

[a]Calculation fit with the use of Eq. (10).
[b]Calculation fit with the use of Eq. (11).

In Eq. (14), N_0 is the number of activator ions in cm^{-3} (concentration of Dy^{3+} ions), e is the electron charge, h is Planck's constant, and $n^- = (n_g + n_m + n_p)/3$ is the averaged refractive index of the crystal (see Table II) at the mean wavelength $\lambda^-_{JJ'}$ of the intermanifold absorption $J \rightarrow J'$ band area. Values of the line strengths, calculated with the use of Eqs. (10) and (11), are listed in Table IX. The intensity parameters Ω_t were obtained by the usual procedure of a minimization of the sum of the squared differences between experimental ($s^{ed}_{JJ'\,exp}$) and calculated ($s^{ed}_{JJ'\,calc}$) line strengths $\Sigma_{J'}(s^{ed}_{JJ'\,exp} - s^{ed}_{JJ'\,calc})^2$ for 13 absorption $^6H_{15/2} \rightarrow J'$ band areas. Both experimental and calculated results together with the rms error of this fitting are presented in Table IX.

Knowing the Ω_t parameters and the corresponding values of $\langle \cdots \| U^{(t)} \| \cdots \rangle$ (from Ref. 65), we calculated the spontaneous probability for all luminescence $J \rightarrow J'$ transitions that originate from the $^4F(3)_{9/2}$ state as

$$A^{ed}_{JJ'} = 64\pi^4 e^2/\{3h(2J+1)\lambda^{-3}_{JJ'}\}[n^-(n^{-2}+2)^2]/9 \times [\Sigma_{t=2,4,6}\Omega_t |\langle 4f^N[SL]J \| U^{(t)} \| 4f^N[S'L']J' \rangle|^2]. \quad (15)$$

The results obtained are given in Table IX. These data permitted us to determine the total spontaneous emission probability $\Sigma_{J'}A^{ed}_{JJ'}$ and the intermanifold branching ratios, defined as

$$\beta_{JJ'} = A^{ed}_{JJ'}/\Sigma_{J'}A^{ed}_{JJ'}. \quad (16)$$

Due to a very large energy gap of ≈7200 cm^{-1} between Stark energy levels of manifolds $^4F(3)_{9/2}$ and $^6F_{1/2}$ (the next lower manifold on the energy scale; see Fig. 4), and the probability of a multiphonon nonradiative channel of $^4F(3)_{9/2} \sim > {}^6F_{1/2}$ we can assume with confidence that $W_{JJ'} \approx 0$. In this case the radiative and luminescence decay times of this initial laser state will be equal:

$$\tau_{rad} = \tau_{lum} = 1/\Sigma_{J'}A^{ed}_{JJ'}. \quad (17)$$

All these calculated characteristics are summarized in Table X. By way of example, in Fig. 18 we show the survey orientational luminescence spectra $^4F(3)_{9/2} \rightarrow J'$ for an α-$KGd(WO_4)_2$:Dy^{3+} crystal, with an indication of the intermanifold branching ratios only for several of the most intense bands. The averaged values of experimental branching ratios $\beta^{expt}_{JJ'}$ for both tungstates are presented in this table as well. It is evident that these luminescence parameters, much like other spectroscopic characteristics of these crystals, are very similar. Figure 19 shows the temperature evolution of the luminescence decay from Stark levels of the

TABLE X. Spectroscopic characteristics determining the intensity of luminescence intermanifold transitions $^4F(3)_{9/2} \rightarrow J'$ of Dy^{3+} ions in monoclinic α-$KGd(WO_4)_2$ and α-$KY(WO_4)_2$ single crystals at 300 K.

Terminal state of $^4F(3)_{9/2} \rightarrow J'$ channel	$\lambda^{-}_{JJ'}$ (μm)	$A^{ed}_{JJ'}$ (s^{-1})		τ^{calc}_{rad} (μs^{-1})		τ^{expt}_{lum} (μs^{-1})	Intermanifold branching ratios[c]			
							α-$KGd(WO_4)_2$			α-$KY(WO_4)_2$
							$\beta^{calc}_{JJ'}$		$\beta^{expt}_{JJ'}$	$\beta^{expt}_{JJ'}$ [d]
		a	*b*	*a*	*b*		*a*	*b*		
$^6H_{15/2}$	≈0.47	556	875				0.089	0.140	≈0.17	≈0.155
$^6H_{13/2}$	≈0.57	4025	3888				0.644	0.622	≈0.69	≈0.70
$^6H_{11/2}$	≈0.67	456	412				0.073	0.064	≈0.065	≈0.073
$[^6H_{9/2}+^6F_{11/2}]$	≈0.76	850	725				0.136	0.116	≈0.045	≈0.047
$[^6F_{9/2}+^6H_{7/2}]$	≈0.85	212	212	160	160	175	0.034	0.034	≈0.02	≈0.015
$^6H_{5/2}$	≈0.93	13	19				0.002	0.003	≈0.0025	≈0.002
$^6F_{7/2}$	≈1.01	87	81				0.014	0.013	≈0.005	≈0.006
$^6F_{5/2}$	≈1.17	51	38				0.008	0.006	≈0.0023	≈0.0016
$^6F_{3/2}$	≈1.29	0	0				0.000	0.000	≈0.0001	≈0.0003
$^6F_{1/2}$	≈1.39	0	0				0.000	0.000	≈0.0001	≈0.0001

[a]Calculated value from Eq. (10).

[b]Calculated value from Eq. (11).

[c]The accuracy of the determination of averaged values $\beta^{expt}_{JJ'}$ for the first five luminescence band areas is no better than 10%. As regards other weak near-IR luminescence bands, the accuracy of the measurements was much worse.

[d]The measured values of $\beta^{expt}_{JJ'}$ for the α-$KY(WO_4)_2$:Dy^{3+} are added for comparison. A similar calculation of the $\beta_{JJ'}$ ratios for the heavy doped crystal α-$KY_{0.9}Dy_{0.1}(WO_4)_2$ shows that about 98% of the emitted density also accounts for first five luminescence band areas (Ref. 44).

metastable state $^4F(3)_{9/2}$ of Dy^{3+} ions, and confirms the spectroscopic similarity of investigated monoclinic tungstates as well. Therefore, we conclude that the determined intensity parameters Ω_t (see Table IX) for the α-$KGd(WO_4)_2$:Dy^{3+} crystal can be used to estimate the corresponding spectroscopic characteristics of Dy^{3+} ions in other crystals of this tungstate family, in particular α-$KY(WO_4)_2$, as well as α-$KDy(WO_4)_2$ (Refs. 33 and 44) and α-$KLu(WO_4)_2$.[6,8,34,40] It should be emphasized here

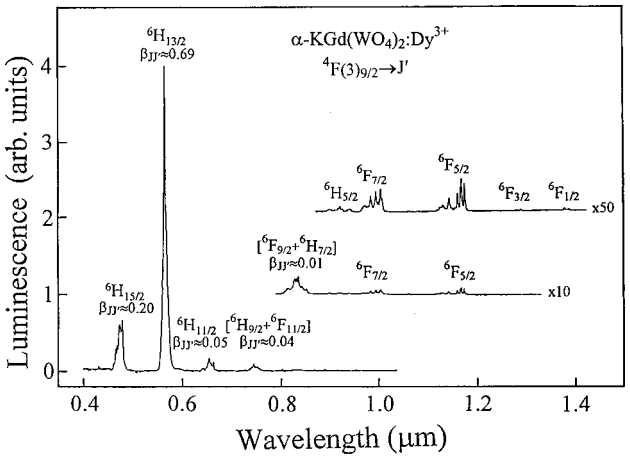

FIG. 18. Survey orientational luminescence spectrum ($^4F(3)_{9/2} \rightarrow J'$ intermanifold transitions, along the *b* axis) of Dy^{3+} ions in an α-$KGd(WO_4)_2$ crystal at 300 K. The values of the corresponding branching ratios ($\beta_{JJ'}$) are given for five channels.

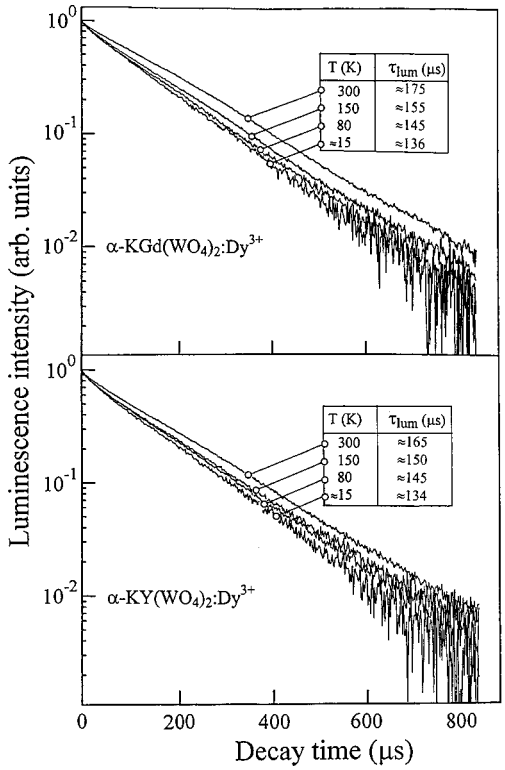

FIG. 19. Temperature evolution of the luminescence decay-time for the metastable state $^4F(3)_{9/2}$ of ≈0.1 at % Dy^{3+}-ions doped into α-$KY(WO_4)_2$ and α-$KGd(WO_4)_2$ crystals.

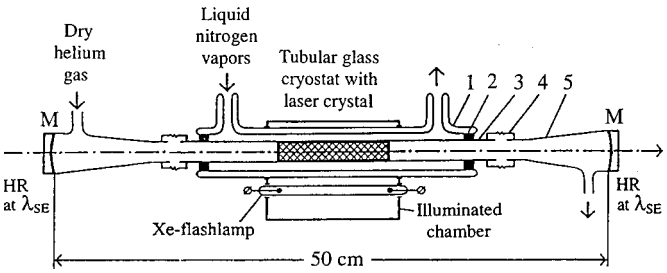

FIG. 20. Fragment of a schematic low-temperature experimental setup for the visible pulsed laser action with monoclinic crystals α-K$R$$(WO_4)_2$:$Dy^{3+}$: (1) tubular glass cryostat, (2) styroform packing, (3) glass tube, (4) gutta-percha connection, and (5) metal conical holder; for other explanations, see the text.

that other lasing Ln^{3+} ions in these crystals behave in an analogous way (see Table I, as well as Refs. 13, 18, 41–43, 45, 47, and 48).

As would be expected in an approximation of intermediate interconfiguration interaction, the accuracy of the description is essentially improved. The additional parameters R_2, R_4, and R_6, obtained during the fitting to the experiment data, differ appreciably from each other. This fact indicates that some excited electronic configurations make an important contribution, and that under these conditions, the use of an approximation of strong interconfiguration interaction does not improve the description of the experimental data.

Before considering SE transitions of Dy^{3+} ions in α-$KY(WO_4)_2$ and α-$KGd(WO_4)_2$ crystals, it is necessary to comment briefly on their luminescence decay dependences $I_{lum}(t)$, which is shown in Fig. 19. It is well known that the theoretical essentials[67,68] of the method of ed intermanifold spectral intensity calculations are based on several simplifying assumptions. Among these are some which practically never agree with the real spectral properties of Ln^{3+}-ion-doped crystals. From this it follows that the population of Stark levels of the initial manifold of the $J \rightarrow J'$ channel should be the same, and that the probabilities of all inter-Stark ed transitions should be equal. For example, in the case of the execution of these conditions the $I_{lum}(t)$ dependences in Fig. 19 could be the same for the indicated temperatures for each crystal. However, the observed temperature evolutions of the luminescence decay incontestably indicates that the probability of inter-Stark transitions from the first level and the four other levels lying above this level of the $^4F(3)_{9/2}$ state of Dy^{3+} ions are noticeably different in the monoclinic tungstates α-$KY(WO_4)_2$ and α-$KGd(WO_4)_2$. Such behaviors of the observed dependences can be explained by a simple expression for the total spontaneous transition probability from a given ith Stark level, taking into account other nearby ith levels, so that

$$A_{\Sigma i} = \{\Sigma_i A_i \exp[-\Delta E_{1i}(^4F(3)_{9/2})/kT]\}/ \{\Sigma_i \exp[-\Delta E_{1i}(^4F(3)_{9/2})/kT]\}, \quad (18)$$

where $\exp[-\Delta E_{1i}(^4F(3)_{9/2})/kT]$ is the Boltzmann factor which characterizes the ith level population; here ΔE_{1i} is the energy gap between the ith level and the lowest (the first) Stark level of the $^4F(3)_{9/2}$ manifold. As follows from this formula, τ_{lum} (or τ_{rad}) will be reduced, if the total spontaneous probability $A_{\Sigma i}$ is larger for the higher lying levels than for the first ($i=1$) level. The lifetime will be increased if the ratio of the $A_{\Sigma i}$ values for these Stark levels is opposite. As is apparent from Fig. 19, the last case agrees exactly with the observed temperature evolution of luminescence decay from the metastable $^4F(3)_{9/2}$ state of Dy^{3+} ions in these tungstates.

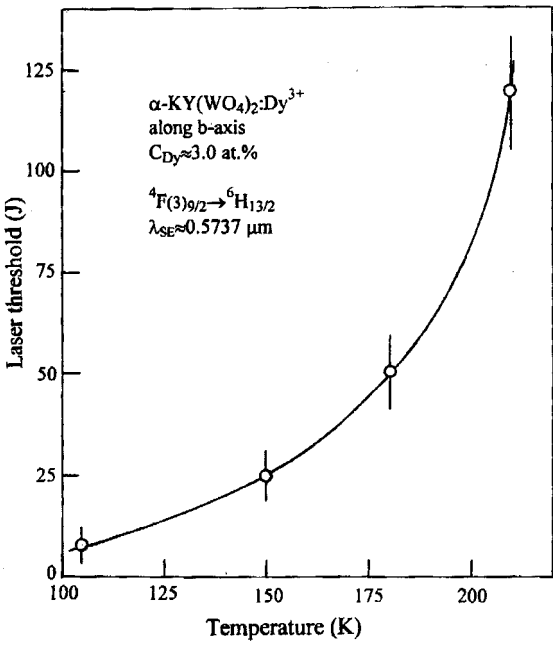

FIG. 21. Dependence of the laser threshold energy on temperature for α-$KY(WO_4)_2$:Dy^{3+} ($C_{Dy} \cong 3.0$ at. %) laser.

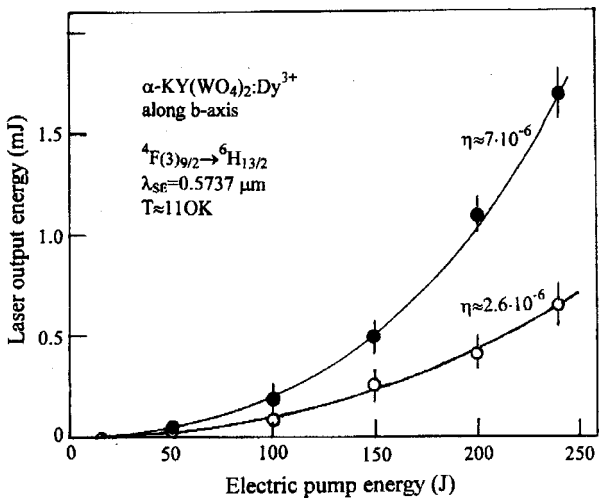

FIG. 22. Dependences of the laser output energy on the electric energy delivered to pump the Xe flashlamp of the α-$KY(WO_4)_2$:Dy^{3+} laser for two concentrations of activator ions. $C_{Dy} \approx 3.0$ at. % (open circles) and $C_{Dy} \approx 1.0$ at. % (filled circles). η is the total efficiency (the ratio of the output laser energy to the electric pump energy).

TABLE XI. Laser parameters and properties for Dy^{3+} ions in monoclinic α-$KY(WO_4)_2$ and α-$KGd(WO_4)_2$ single crystals.

Crystal (orientation)[a]	C_{Dy}[b] (at. %)	SE channel	T (K)	λ_{SE}[c] (μm)	E_{thr}[d] (J)	E_{term}[e] (cm^{-1})	$\Delta\nu_{lum}$ (cm^{-1})	$\sigma^{ef}_{e,ij}$[f] (10^{-19} cm^2)
α-$KY(WO_4)_2$[g]	$\approx$1.0	$^4F(3)_{9/2}\rightarrow{}^6H_{13/2}$	$\approx$110	0.5737	15	$\approx$3565	$\approx$1.5	53$\pm$5
(along the *b* axis)			$\approx$180		110		$\approx$5	13$\pm$6
	$\approx$3.0		$\approx$110		15		$\approx$1.5	53$\pm$5
			$\approx$210		120		$\approx$7	9$\pm$7
	$\approx$1.0	$^4F(3)_{9/2}\rightarrow{}^6H_{11/2}$	$\approx$110	0.6637	120	$\approx$5929	$\approx$2	1.1$\pm$0.5
	$\approx$3.0		$\approx$110		55		$\approx$2.5	
α-$KGd(WO_4)_2$	$\approx$1.0	$^4F(3)_{9/2}\rightarrow{}^6H_{13/2}$	$\approx$110	0.5734	25	$\approx$3565	$\approx$1.5	53$\pm$8
(along the *b* axis)			$\approx$150		100		$\approx$4	19$\pm$6

[a]The direction of the laser axis of the crystalline rod.
[b]Concentration of Dy^{3+} ions in the melt. The segregation coefficient for Dy^{3+} ions in monoclinic tungstates α-$KR(WO_4)_2$ is very close to unity.
[c]λ_{SE} is the wavelength; the measurement accuracy is $\pm$0.0003 μm.
[d]Threshold energy in joules.
[e]E_{term} is the laser terminal Stark level.
[f]Calculated value for the cross section.
[g]For this crystal we give improved experimental data.

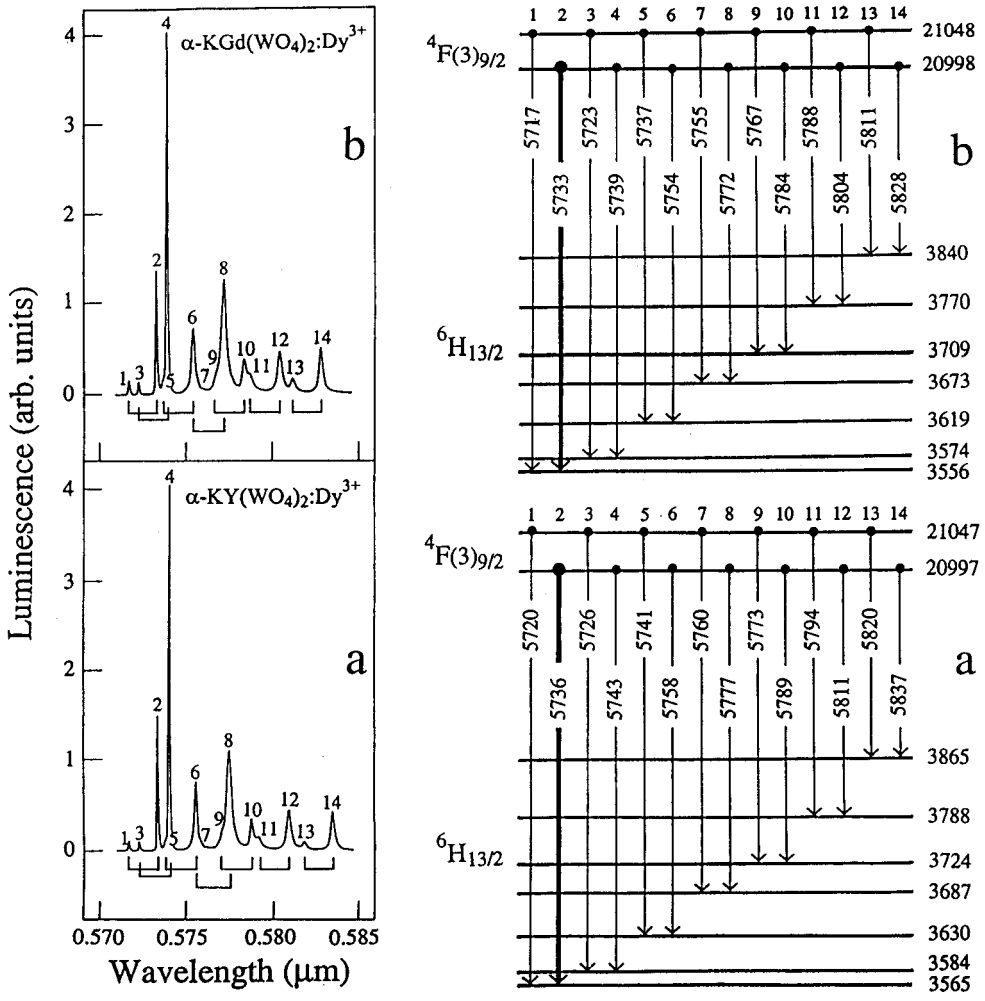

FIG. 23. Orientational luminescence spectra ($^4F(3)_{9/2}\rightarrow{}^6H_{13/2}$ laser channel, along the *a* axis) and CF splitting schemes of Dy^{3+} ions in (a) α-$KY(WO_4)_2$ and (b) α-$KGd(WO_4)_2$ crystals at $\approx$15 K. Thick arrows in the energy schemes indicate the transitions at which laser action was excited. Other notations are the same as in Figs. 5 and 6.

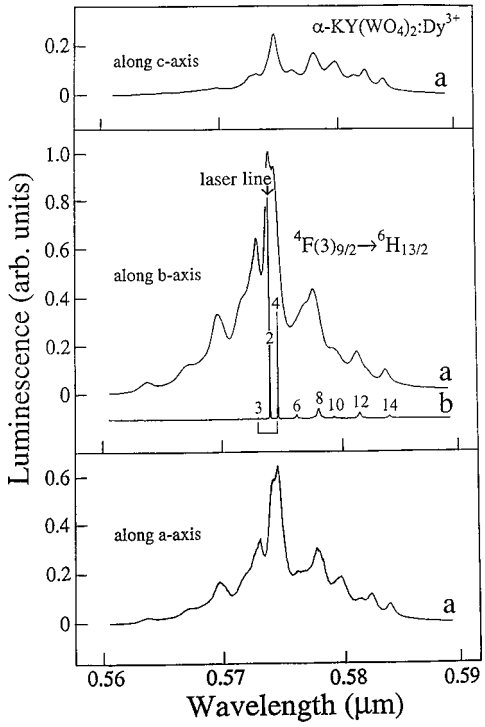

FIG. 24. Orientational luminescence spectra ($^4F(3)_{9/2}\rightarrow{}^6H_{13/2}$ laser channel) of Dy^{3+} ions in an α-$KY(WO_4)_2$ crystal at (a) 300 K and (b) ≈15 K. The numeration of lines in spectrum (b) is the same as in Fig. 23.

Therefore, results obtained for calculated τ_{rad}^{calc} by the use of Eqs. (10) and (11) and measured τ_{lum}^{exp} values given in Table X should be compared only with regard to the above-mentioned consideration.

VI. STIMULATED EMISSION PROPERTIES

In our SE investigations of Dy^{3+}-activator ions in α-$KY(WO_4)_2$ and α-$KGd(WO_4)_2$ tungstates, that involved pulsed free-running mode laser action in the "yellow" ($^4F(3)_{9/2}\rightarrow{}^6H_{13/2}$) and "red" ($^4F(3)_{9/2}\rightarrow{}^6H_{11/2}$) channels, we excited fairly weak absorption bands observed between ≈0.38 and ≈0.47 μm in order to avoid undesirable color center formation. We used filtered emission from a Xe flashlamp of ISP-250 type ($\tau_{exc}\approx 100\ \mu s$) in an illuminating chamber of elliptical cross section with Ag-coated inner reflected surfaces. Figure 20 shows how the crystalline lasing rod was centrally positioned inside a tubular glass made from a ZhS-15 type glass that is transparent from ≈0.36 μm cryostat, where the temperature could be lowered to ≈110 K by flowing liquid-nitrogen vapor. We used a confocal optical cavity that consisted of changeable spherical ($r=500$ mm) multilayer dielectric mirrors with ≈0.5% transmission, which ensured a high Q factor at SE wavelengths. The spectral composition of the laser action achieved in the visible of Dy^{3+}-ion-doped monoclinic tungstates was measured with a grating monochromator of MDR-3 type. We also used an oscillographic recording system equipped with an avalanche Si photodiode. The threshold E_{thr} and output energies of the observed visible SE were evaluated with the same experimental technique. For the "yellow" SE transition of α-$KY(WO_4)_2$:Dy^{3+} crystals, in Figs. 21 and 22 we show the dependences of laser threshold on temperature and laser output energy on electric energy delivered to the Xe-flashlamp pump, respectively. Selected results of these measurements for both crystals are listed in Table XI.

Under these nonoptimal pumping conditions, we obtained pulsed SE only at cryogenic temperatures on our crystals that contained relatively small Dy^{3+}-ion concentrations. Results

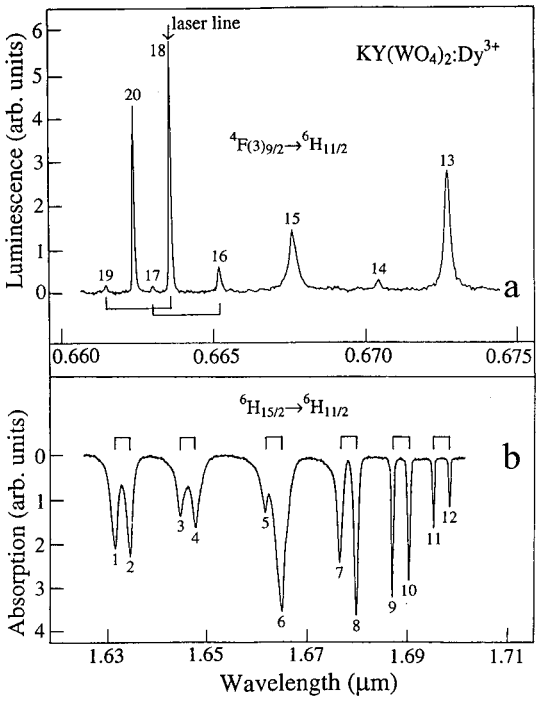

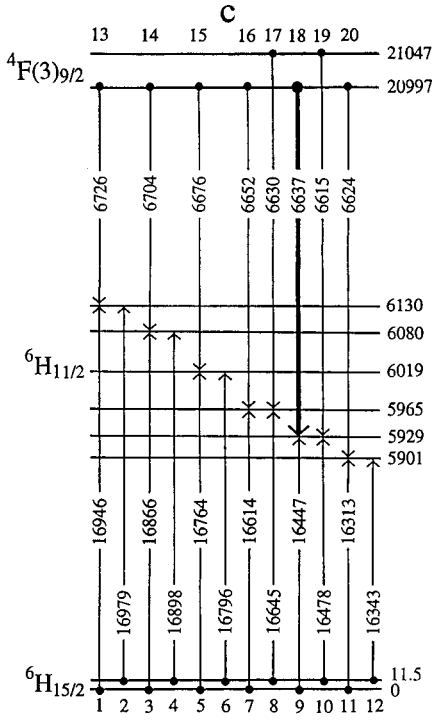

FIG. 25. Orientational luminescence spectrum ($^4F(3)_{9/2}\rightarrow{}^6H_{11/2}$ laser channel, along the *b* axis). (b) Unpolarized absorption spectrum ($^6H_{15/2}\rightarrow{}^6H_{11/2}$) and CF splitting of the $^4F(3)_{9/2}$, $^6H_{15/2}$, and $^6H_{11/2}$ manifolds of Dy^{3+} ions in an α-$KY(WO_4)_2$ crystal at ≈15 K. The thick arrow in the energy scheme indicates the transition at which laser action was obtained. Other notations are the same as in Figs. 5 and 6.

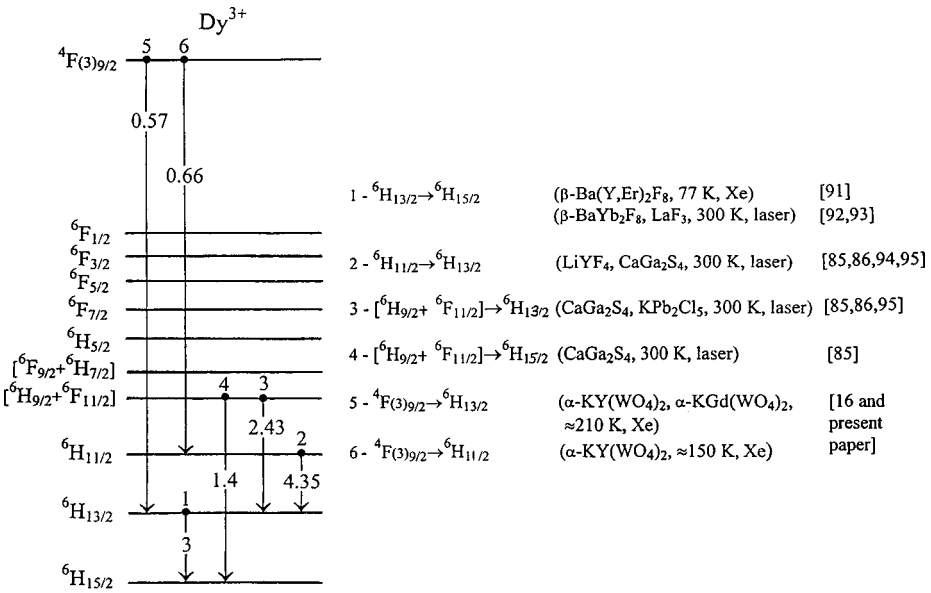

FIG. 26. SE channels of Dy^{3+} ions in insulating laser crystals are given along with the crystal names and the working temperature and excitation method (Xe denotes the flashlamp pumping, and laser pumping by laser emission). Other notations are the same as in Fig. 1.

of the identification of observed low-threshold ''yellow'' laser emission ($^4F(3)_{9/2}\rightarrow{}^6H_{13/2}$ channel) for these two monoclinic tungstates are presented in Fig. 23. Here again, as in Fig. 6 we show luminescence spectra of these crystals also recorded along the *a* axis which give more informative pictures for a vision of a maximal possible number of peaks that explains all inter-Stark transitions at ≈15 K from the two lowest levels of metastable state $^4F(3)_{9/2}$. The set of luminescence spectra recorded along three main crystallographic axes, in particular, along the *b* axis which corresponds to the laser direction exactly, can be found in Fig. 24. The identification of the ''red'' SE ($^4F(3)_{9/2}\rightarrow{}^6H_{11/2}$ channel) for an α-$KY(WO_4)_2$:Dy^{3+} crystal is also shown in Fig. 25. As we see from Figs. 23 and 25, all excited SE transitions originate from the lowest Stark level of the $^4F(3)_{9/2}$ state. A detailed analysis of the intensity characteristics of these luminescence channels shows that at other orientations of these crystals SE can also be available at wavelengths of the other inter-Stark transitions.

Due to a noticeable overlapping of the strongest lines with their neighbors in the luminescence channels $^4F(3)_{9/2}\rightarrow{}^6H_{13/2}$ and $^4F(3)_{9/2}\rightarrow{}^6H_{11/2}$ (see Figs. 6 and 7), at wavelengths for which we have excited SE at a temperature interval from ≈110 to ≈210 K (see Table XI), we have estimated the values of effective ($\sigma^{\rm ef}_{e,ij}$) and peak ($\sigma^{p}_{e,ij}$) cross sections for the wavelength of inter-Stark laser transitions by the formula

$$\sigma^{\rm ef}_{e,ij}=\sigma^{p}_{e,ij}+\Sigma_{(imjm)\neq(ij)}p^{imjm}_{ij}\sigma^{p}_{e,imjm}, \tag{19}$$

where

$$\sigma^{p}_{e,ij}=\lambda^2_{\rm SE}\beta^{\rm or}_{ij}/4\pi^2 n^{-2}\Delta\nu_{\rm lum}\tau_{\rm rad}$$
$$=(\lambda^2_{\rm SE}/4\pi^2 n^{-2}\Delta\nu_{\rm lum})(\beta^{\rm or}_{ij}\Sigma_i b_i/\tau_{\rm rad}b_i). \tag{20}$$

Eqs. (19) and (20), p^{imjm}_{ij} is the coefficient characterizing the overlap of the neighboring lines of the $i_m\rightarrow j_m$ transition and the line of a given SE inter-Stark transition $i\rightarrow j$; $\Delta\nu_{\rm lum}$ is the luminescence linewidth, n^- is the average refractive index of the crystal at the SE wavelength $\lambda_{\rm SE}$, $\beta^{\rm or}_{ij}$ is the orientational inter-Stark luminescence branching ratio, and b_i is the same Boltzmann factor as we used in Eq. (14). For determining $\beta^{\rm or}_{ij}$ values, we used the measured intermanifold branching ratios which are given in Table X. The relation between these branching ratios is given as

$$\beta_{ij}=\tfrac{1}{3}\Sigma_{a,b,c}\Sigma_{i,j}\beta^{\rm or}_{ij}. \tag{21}$$

The values of $\beta^{\rm or}_{ij}$ ratios and p^{imjm}_{ij} coefficients, as well as luminescence linewidths $\Delta\nu_{\rm lum}$ required for the calculation of the peak cross sections at the SE wavelengths, have been extracted by a decomposition of the corresponding orientational intermanifold luminescence spectra. One of them, for example, is shown in Fig. 24. Results from the calculation of the peak cross sections $\sigma^{p}_{e,ij}$ for the visible SE at wavelengths of two lasing intermanifold channels are presented in Table XI for $^4F(3)_{9/2}\rightarrow{}^6H_{13/2}$ and $^4F(3)_{9/2}\rightarrow{}^6H_{11/2}$ of Dy^{3+} ions in monoclinic tungstates α-$KY(WO_4)_2$ and α-$KGd(WO_4)_2$.

VII. CONCLUSION

Monoclinic tungstates α-$KY(WO_4)_2$ and α-$KGd(WO_4)_2$ were grown doped with Dy^{3+} ions. We carried out a complex characterization of their crystallographic, optical, and stimulated-emission properties. Based on these investigations, we consider the Dy^{3+} ion to be a promising activator in crystals for ''yellow'' $^4F(3)_{9/2}\rightarrow{}^6H_{13/2}$ and ''red'' $^4F(3)_{9/2}\rightarrow{}^6H_{11/2}$ lasing. Our experiments extend the laser potential of Dy^{3+} doped crystals. It is now possible to excite SE on six intermanifold $4f^9$-$4f^9$ channels (Fig. 26) in a relatively wide spectral range from ≈0.57 to ≈4.35 μm. It is beyond all shadow of a doubt that other SE channels will soon be discovered in crystals with Dy^{3+} ions. These channels will involve both visible and mid-IR spectral regions.

ACKNOWLEDGMENTS

The Russian authors gratefully acknowledge partial financial support from the Russian Foundation for Basic Research, as well as the State Scientific Programs ''Fundamental Metrology'' and ''Fundamental Spectroscopy.'' We wish to acknowledge here P. V. Klevtsov, who made a significant contribution during at the initial stages of the investigations of the α-$KR(WO_4)_2$ monoclinic tungstates. We also wish to thank J. Hanuza, A. V. Butashin, A. F. Konstantinova, and T. H. Chyba for their participation in making optical measurements and for fruitful discussions. The work at San Jose State University was supported by the Institute for Modern Optics. The work at Hampton University was supported by NASA through Grant No. NCC-1-251, where J. C. Barnes rendered perceptible assistance. All the authors agree that the investigations were considerably aided thanks to the cooperation of the Joint Open Laboratory for Laser Crystals and Precise Laser Systems.

*Email address: kaminalex@mail.ru

†Email address: jbgruber@email.sjsu.edu

‡Email address: ueda@ils.uec.ac.jp

[1] A. A. Kaminskii, P. V. Klevtsov, and A. A. Pavlyuk, Phys. Status Solidi A **5**, K79 (1971).

[2] A. A. Kaminskii, P. V. Klevtsov, L. Li, and A. A. Pavlyuk, IEEE J. Quantum Electron. **8**, 457 (1971).

[3] A. A. Kaminskii, A. A. Pavlyuk, P. V. Klevtsov, I. F. Balashov, V. A. Berenberg, S. E. Sarkisov, V. A. Fedorov, M. A. Petrov, and V. V. Lyubchenko, Izv. Akad. Nauk SSSR, Neorgan. Mater. **13**, 582 (1977).

[4] A. A. Kaminskii, A. A. Pavlyuk, I. F. Balashov, V. A. Berenberg, V. V. Lyubchenko, V. A. Fedorov, T. I. Butaeva, and L. I. Bobovich, Izv. Akad. Nauk SSSR Neorgan. Mater. **13**, 1541 (1977).

[5] A. A. Kaminskii, A. A. Pavlyuk, I. F. Balashov, V. A. Berenberg, V. V. Lyubchenko, V. A. Fedorov, T. I. Butaeva, and L. I. Bobovich, Izv. Akad. Nauk SSSR, Neorgan. Mater. **14**, 2256 (1978).

[6] A. A. Kaminskii, A. A. Pavlyuk, N. R. Agamalyan, L. I. Bobovich, A. V. Lukin, and V. V. Lyubchenko, Izv. Akad. Nauk SSSR, Neorgan. Mater. **15**, 1496 (1979).

[7] A. A. Kaminskii, A. A. Pavlyuk, T. I. Butaeva, L. I. Bobovich, and V. V. Lyubchenko, Izv. Akad. Nauk SSSR, Neorgan. Mater. **15**, 541 (1979).

[8] A. A. Kaminskii, A. A. Pavlyuk, N. R. Agamalyan, S. E. Sarkisov, L. I. Bobovich, A. V. Lukin, and V. V. Lyubchenko, Izv. Akad. Nauk SSSR, Neorgan. Mater. **15**, 2092 (1979).

[9] A. A. Kaminskii, A. A. Pavlyuk, Ch. Ngok, L. I. Bobovich, V. A. Fedorov, and V. V. Lyubchenko, Dokl. Akad. Nauk SSSR **245**, 575 (1979) [Sov. Phys. Dokl. **24**, 201 (1979)].

[10] A. A. Kaminskii, A. G. Petrosyan, V. A. Fedorov, S. E. Sarkisov, V. V. Ryabchenkov, A. A. Pavlyuk, V. V. Lyubchenko, and I. V. Mochalov, Dokl. Akad. Nauk SSSR **260**, 64 (1981) [Sov. Phys. Dokl. **26**, 846 (1981)].

[11] A. A. Kaminskii, A. A. Pavlyuk, A. I. Polyakova, and V. V. Lyubchenko, Dokl. Akad. Nauk SSSR **268**, 856 (1983) [Sov. Phys. Dokl. **28**, 154 (1983)].

[12] A. A. Kaminskii, S. N. Bagayev, and A. A. Pavlyuk, Phys. Status Solidi A **151**, K53 (1995).

[13] The laser action of Yb^{3+} ions in α-$KY(WO_4)_2$ and α-$KGd(WO_4)_2$ was reported during the International Symposium on Modern Problem of Laser Physics (Novosibirsk, September 1996) by A. A. Kaminskii (unpublished), and also as his oral comments during International Conference Euro/CLEO-97 (Humburg). The first paper on laser action of these crystals was published by A. V. Kuleshov, A. A. Lagatsky, A. V. Podlipensky, V. P. Mikhailov, and G. Huber, Opt. Lett. **22**, 1317 (1997).

[14] A. A. Kaminskii and A. A. Pavlyuk, Neorgan. Mater. (Russia) **31**, 1500 (1995).

[15] A. A. Kaminskii, L. Li, A. V. Butashin, V. S. Mironov, A. A. Pavlyuk, S. N. Bagayev, and K. Ueda, Jpn. J. Appl. Phys. **36**, LI07 (1997).

[16] A. Kaminskii, U. Hömmerich, D. Temple, J. T. Seo, K. Ueda, S. Bagayev, and A. Pavlyuk, Jpn. J. Appl. Phys. **39**, L208 (2000).

[17] A. Pavlyuk, L. Kozeeva, K. Fomin, V. Gladyshev, V. Gulyanov, V. Pivtsov, and A. Kaminskii, Izv. Akad. Nauk SSSR, Neorgan. Mater. **19**, 848 (1983).

[18] A. A. Kaminskii, *Crystalline Lasers: Physical Processes and Operating Schemes* (CRC Press, Boca Raton, FL, 1996).

[19] M. J. Weber, *Handbook of Laser Wavelengths* (CRC Press, Boca Raton, FL, 2000).

[20] A. A. Kaminskii, A. I. Bodretsova, A. G. Petrosyan, and A. A. Pavlyuk, Sov. J. Quantum Electron. **13**, 975 (1983).

[21] A. A. Mak, V. O. Fromzel, and A. O. Shcherbakov, Izv. Akad. Nauk SSSR, Fiz. **48**, 1466 (1984).

[22] A. A. Kaminskii, H. R. Verdun, W. Koechner, F. A. Kuznetsov, and A. A. Pavlyuk, Kvant. Electron. (Moscow) **9**, 941 (1992) [Sov. J. Quantum Electron. **22**, 875 (1992)].

[23] K. Kushawaha, A. Banerjee, and L. Major, Appl. Phys. B: Photophys. Laser Chem. **56**, 239 (1993).

[24] J. M. Esmeria, H. Ishii, M. Sato, and H. Ito, Opt. Lett. **20**, 1538 (1995).

[25] L. Major, Y. Chen, Y. Yan, K. Sentrayan, and V. Kushawaha, in *Proceedings of the International Conferences* (STS Press, McLean, VA, 1996), p. 851.

[26] O. Musset and J. P. Boquillon, in *Advanced Solid State Lasers* (OSA, Washington, DC, 1997), Vol. 10, p. 300.

[27] A. A. Demidovich, A. P. Shkadarevich, M. B. Danailov, P. Apai, T. Gasmi, V. P. Gribkovskii, A. N. Kuzmin, G. I. Ryabstev, and L. E. Batay, Appl. Phys. B: Photophys. Laser Chem. **67**, 11 (1998).

[28] F. Brunner, G. J. Spuhler, J. Aus der Au, L. Krainer, F. Morier-Genoud, R. Paschotta, N. Lichtenstein, S. Weiss, C. Harder, A. A. Lagatsky, A. Abdolvand, N. V. Kuleshov, and U. Keller, Opt. Lett. **25**, 1119 (2000).

[29] A. M. Ivanyuk, P. A. Shachverdov, V. D. Belyev, M. A. Ter-Pogosyan, and V. L. Ermolaev, Opt. Spectrosk. **59**, 950 (1985) [Opt. Spectrosc. (USSR) **58**, 589 (1985)].

[30] K. Andryunas, Yu. Vishchakas, V. Kabelka, I. V. Mochalov, A. A. Pavlyuk, G. T. Petrovskii, and V. Syrus, Zh. Eksp. Teor. Fiz. Pis'ma **42**, 33 (1985) [Sov. Phys. JETP **42**, 410 (1985)].

[31] A. A. Kaminskii, Kvant. Elektron. (Moscow) **20**, 532 (1993).
[32] K. A. Stankov and G. Marawsky, Appl. Phys. B: Photophys. Laser Chem. **61**, 213 (1995).
[33] J. T. Murray, R. C. Powell, and N. Peyghambarian, J. Lumin. **66–67**, 89 (1996).
[34] A. A. Kaminskii, K. Ueda, H. J. Eichler, J. Findeisen, S. N. Bagayev, F. A. Kuznetsov, A. A. Pavlyuk, G. Boulon, and F. Bourgeois, Jpn. J. Appl. Phys. **37**, L923 (1998).
[35] J. Findeisen, H. J. Eichler, and A. A. Kaminskii, IEEE J. Quantum Electron. **35**, 173 (1999).
[36] A. A. Lagatsky, A. Abdolvand, and N. V. Kuleshov, Opt. Lett. **25**, 616 (2000).
[37] A. A. Kaminskii, N. S. Ustimenko, A. V. Gulin, S. N. Bagaev, and A. A. Pavlyuk, Dokl. Akad. Nauk **359**, 179 (1998) [Sov. Phys. JETP **43**, 148 (1998)].
[38] A. A. Kaminskii, P. V. Klevtsov, L. Li, and A. A. Pavlyuk, Izv. Akad. Nauk SSSR, Neorgan. Mater. **12**, 2153 (1972).
[39] A. A. Kaminskii, S. E. Sarkisov, A. A. Pavlyuk, and V. V. Lyubchenko, Izv. Akad. Nauk SSSR, Neorgan. Mater. **16**, 720 (1980).
[40] A. A. Kaminskii, N. R. Agamalyan, A. A. Pavlyuk, L. I. Bobovih, and V. V. Lyubchenko, Izv. Akad. Nauk SSSR, Neorgan. Mater. **19**, 982 (1983).
[41] J. J. Wang, X. Z. You, and A. B. Dai, Chinese J. of Chem. **10**, 289 (1992).
[42] Y. Huang, Z. Luo, and G. Wang, Opt. Commun. **88**, 42 (1992).
[43] A. A. Kaminskii, L. Li, A. V. Butashin, V. S. Mironov, A. A. Pavlyuk, S. N. Bagayev, and K. Ueda, Opt. Rev. (Japan) **4**, 309 (1997).
[44] L. Macalik, J. Hanuza, B. Macalik, W. Ryba-Romanowski, S. Golab, and A. Pietraszko, J. Lumin. **79**, 9 (1998).
[45] N. V. Kuleshov, A. A. Lagatsky, A. V. Podlipensky, V. P. Mikhailov, A. A. Kornienko, E. B. Dunina, S. Hartung, and G. Huber, J. Opt. Soc. Am. B **15**, 1205 (1998).
[46] F. Bourgeois, A. Brenier, G. Metrat, N. Muhlstein, and G. Boulon, Eur. Phys. J. A **6**, 155 (1999).
[47] M. C. Pujol, M. Rico, C. Zaldo, R. Sole, V. Nikolov, X. Solans, M. Aguilo, and F. Diaz, Appl. Phys. B: Photophys. Laser Chem. **68**, 187 (1999).
[48] C. Zaldo, M. Rico, C. Cascales, M. C. Pujol, J. Massons, M. Auguilo, F. Diaz, and P. Porcher, J. Phys.: Condens. Matter **12**, 8531 (2000).
[49] M. A. Elyashevich, *Spectra of Rare Earths* (Gosttekhteorizdat, Moscow 1953), also see, the translation USEAC, AEC-tr-4403, Office of Technical Information, Department of Commerce, Washington, DC, 1961.
[50] G. H. Dieke, *Spectra and Energy Levels of Rare Earth Ions in Crystals* (Wiley, New York 1968).
[51] C. A. Morrison and R. P. Leavitt, in *Handbook on the Physics and Chemistry of Rare-Earths*, edited by K. A. Gschneider and L. Eyring (North-Holland, Amsterdam, 1982), Vol. 5, p. 461.
[52] J. L. Fray, H. H. Caspers, H. E. Rast, and S. A. Miller, J. Chem. Phys. **48**, 2342 (1968).
[53] C. A. Morrison and R. P. Leavitt, J. Chem. Phys. **71**, 2366 (1979).
[54] P. V. Klevtsov and L. P. Kozeeva, Sov. Phys. Dokl. **13**, 185 (1969).
[55] A. A. Kaminskii, A. F. Konstantinova, A. V. Butashin, and A. A. Pavlyuk, Kristallographiya **46**, 722 (2001) [Sov. Phys. Crystallogr. **46**, 665 (2001)].
[56] A. A. Kaminskii, C. L. McCray, H. R. Lee, S. W. Lee, D. A. Temple, T. H. Chyba, W. D. Marsh, J. C. Barnes, A. N. Annanenkov, V. D. Legun, H. J. Eichler, G. M. A. Gad, and K. Ueda, Opt. Commun. **183**, 277 (2000).
[57] V. A. Berenberg, S. N. Karpukhin, and I. V. Mochalov, Sov. J. Quantum Electron. **17**, 1178 (1987).
[58] *International Tables for Crystallography*, edited by T. Hanh (Reidel, Dordrecht, 1992), Vol. A.
[59] N. Karayianis, J. Chem. Phys. **56**, 3734 (1972), and references therein.
[60] P. V. Klevtsov, L. P. Kozeeva, and A. A. Pavlyuk, Sov. Phys. Crystallogr. **20**, 732 (1976).
[61] S. Fraga, K. M. Saxema, and J. Karwowski, in *Physical Science Data: 5. Handbook of Atomic Data* (Elsevier, New York 1976).
[62] P. C. Schmidt, A. Weis, and T. P. Das, Phys. Rev. B **19**, 5525 (1979).
[63] C. A. Morrison, R. P. Leavitt, and D. E. Wortman, J. Chem. Phys. **73**, 2580 (1980).
[64] J. B. Gruber, B. Zandi, and M. F. Reid, Phys. Rev. B **60**, 15 643 (1999).
[65] W. T. Carnall, P. R. Fields, and K. Rajnak, J. Chem. Phys. **49**, 4412 (1968); **49**, 4424 (1968); **49**, 4443 (1968); **49**, 4450 (1968).
[66] N. C. Chang, J. B. Gruber, R. P. Leavitt, and C. A. Morrison, J. Chem. Phys. **76**, 3877 (1982).
[67] B. R. Jadd, Phys. Rev. **127**, 750 (1962).
[68] G. S. Offelt, J. Chem. Phys. **37**, 511 (1962).
[69] R. D. Peacock, Struct. Bonding (Berlin) **22**, 83 (1975).
[70] J. D. Axe, J. Chem. Phys. **39**, 1154 (1963).
[71] W. F. Krupke and J. B. Gruber, Phys. Rev. **139**, 2008 (1965).
[72] W. F. Krupke, Phys. Rev. **145**, 325 (1966).
[73] M. J. Weber, Phys. Rev. **157**, 262 (1967).
[74] M. J. Weber, Phys. Rev. **171**, 183 (1968).
[75] J. R. Chamberlain, A. C. Everitt, and J. W. Orton, J. Phys. C **1**, 157 (1968).
[76] W. F. Krupke, IEEE J. Quantum Electron. **7**, 153 (1971).
[77] M. J. Weber, B. H. Matsinger, V. L. Donlan, and G. T. Surrat, J. Chem. Phys. **57**, 562 (1972).
[78] M. J. Weber, T. E. Waritimos, and B. H. Matsinger, Phys. Rev. B **8**, 47 (1973).
[79] A. A. Kaminskii and L. Li, Phys. Status Solidi A **26**, K21 (1974).
[80] W. F. Krupke, Opt. Commun. **12**, 210 (1974).
[81] B. G. Wybourne, *Spectroscopic Properties of Rare Earths* (Wiley, New York, 1965).
[82] B. R. Judd, J. Chem. Phys. **44**, 281 (1966).
[83] C. K. Jorgensen and B. R. Judd, Mol. Phys. **8**, 281 (1964).
[84] B. M. Antipenko, Opt. Spektrosk. **56**, 72 (1984) [Opt. Spectrosc. (USSR) **56**, 44 (1984)].
[85] M. C. Nostrand, R. H. Page, S. A. Pyane, W. F. Krupke, and P. G. Schunemann, and L. I. Isaenko, in *Advanced Solid State Lasers* (OSA, Washington, DC, 1998), Vol. 19, p. 524.
[86] M. C. Nostrand, R. H. Page, S. A. Payne, W. F. Krupke, P. G. Schunemann, and L. I. Isaenko, in *Advanced Solid State Lasers* (OSA, Washington, DC, 1999), Vol. 26, p. 441.
[87] A. A. Kaminskii, U. Hömmerich, D. Temple, J. T. Seo, and A. A. Pavlyuk, Phys. Status Solidi A **174**, R7 (1999).
[88] A. A. Kornienko, A. A. Kaminskii, and E. B. Dunina, Phys. Status Solidi B **157**, 267 (1990).

[89] A. A. Kornienko, E. B. Dunina, and V. L. Yankevich, Opt. Spektrosk. **81**, 871 (1996) [Opt. Spectrosc. **81**, 871 (1996)].
[90] P. Goldner and F. Auzel, J. Appl. Phys. **79**, 7972 (1996).
[91] L. F. Johnson and H. J. Guggenheim, Appl. Phys. Lett. **23**, 96 (1973).
[92] B. M. Antipenko and A. A. Mak, in *Proceedings of the Conference on Laser Optics* (Optical State Institute, Leningrad, 1980), p. 234.
[93] N. Djeu, V. E. Hartwell, A. A. Kaminskii, and A. V. Butashin, Opt. Lett. **22**, 997 (1997).
[94] N. P. Barnes, L. Esterowitz, and R. Allen, in *Technical Digest Papers Conference on Lasers and Electro-Optics* (OSA, Washington DC, 1984), p. 5.
[95] M. C. Nostrand, R. H. Page, S. A. Payne, P. G. Schunemann, and L. I. Isaenko, in *Advanced Solid State Lasers* (OSA, Washington DC, 2000), Vol. 34, p. 459.